Acoustic data-driven framework for structural defect reconstruction: A manifold learning perspective

Qi Li[1], Fushun Liu[2], Peng Li[1], Bin Wang[1], Zhenghua Qian[1,*], Dianzi Liu[3,*]

[1]*State Key Laboratory of Mechanics and Control of Mechanical Structures, College of Aerospace Engineering, Nanjing University of Aeronautics and Astronautics, Nanjing, 210016, China*

[2]*College of Engineering, Ocean University of China, Qingdao 266100, China*

[3]*School of Engineering, University of East Anglia, UK*

[*] Corresponding authors, E-mail: qianzh@nuaa.edu.cn; Dianzi.liu@uea.ac.uk

Abstract:

Data-driven quantitative defect reconstruction using ultrasonic guided waves has recently demonstrated great potential in the area of non-destructive testing (NDT) and structural health monitoring (SHM). In this paper, a novel deep learning-based framework, called Deep-guide, has been proposed to convert the inverse guided wave scattering problem into a data-driven manifold learning progress for defect reconstruction. The architecture of Deep-guide network consists of the efficient encoder-projection-decoder blocks to automatically realize the end-to-end mapping of noisy guided wave reflection coefficients in the wavenumber domain to defect profiles in the spatial domain by the manifold distribution principle and intelligent learning. Towards this, results by the modified boundary element method for efficient calculations of scattering fields of guided waves have been generated as acoustic emission signals of the Deep-guide to facilitate the training and extract the features homeomorphically. The correctness, robustness and efficiency of the proposed framework have been demonstrated throughout several examples and experimental tests of circular defects. It has been noted that Deep-guide has the ability to achieve the high-quality defect reconstructions and provides valuable insights into the development of effective data-driven techniques for structural health monitoring and complex defect reconstructions.

Keywords: Manifold learning, Acoustic Data-driven, Guided wave, Defect reconstruction

1.Introduction

Ultrasonic guided waves (UGW) have been widely used in non-destructive testing (NDT), due to their superb inspection sensitivity and capability of traveling large distances without much attenuation[1-4]. Applying the mode control and frequency tuning techniques, researchers have enabled UGW to achieve the high-precision and long-distance detection with just 1 or 2 probes in a variety of unusual circumstances such as inspections under fluids, coatings, and insulation[5]. In general, the use of UGW to reconstruct structural defects can be attributed to an inverse scattering problem. Solutions to such problem have focused on the development of knowledge-driven or physical-analytical methods, which are based on the guided wave scattering theory to realize the mapping between characteristics of the scattered waves and the defect profiles.

For the detection of defects in plate-like structures, Rose et al[6] deduced a dyadic Green's function for a point moment/force in a plate using the Mindlin plate model. Employing the Born approximation, a relationship between the far-field scattering amplitude and the spatial Fourier transform was found to reconstruct the weak flexural inhomogeneity[7]. Subsequently, the far-field approximation-based approaches to the quantitative reconstruction of plate thinnings in solving the inverse problems were developed using SH-waves[8] and Lamb waves[9], respectively. In 2011, a two-dimensional finite element (FE)-based inverse scheme was proposed to size strip-like defects in plates using guided Lamb wave modes for the known defect position along the plate guide[10]. This technique was also applied for the determination of a cracked zone, which was representative of a uniform and linear impact damage inside a composite plate[11]. In the field of defect detection in pipelines, Da et al[12] proposed a novel method (QDFT) for the quantitative reconstruction of pipeline defects using ultrasonic guided SH-waves. This method started from the boundary integral equation and derived the Fourier transform pair of the defect shape function and reflection coefficients using the Born approximation. Finally, the unknown defect was reconstructed throughout the reference model.

Despite the successful realization of quantitative defect reconstructions, there are some limitations for such knowledge-driven approaches. First, the inverse model is usually an approximate description of the reality, and extending it might be challenging due to the multi-mode and dispersive properties of guide waves[13]. Relatively accurate analytical models, such as those based on the iterative optimization, hardly demonstrated the real-time capabilities due to the computational complexity; Second, as the scattered signals often contain noise, the signal processing has to be conducted to solve such the ill-posed inverse scattering problem using the knowledge-driven mode[12].

Taking into account these facts, the data-driven method has been introduced to solve the guided waves scattering problem and also has widespread impacts on the strategies of problem solving in many diverse fields, including inverse reconstructions[14-17]. For example, Feng et al[18] proposed a general end-to-end deep learning-based 3D reconstruction framework, which stochastically reconstructed a three-dimensional (3D) structure of porous media from a given two-dimensional (2D) image. In[19], the potential of carrying out inverse problems with linear and non-linear behaviour using deep learning methods was investigated. Besides, Florent et al[20] addressed the inverse identification of apparent elastic properties of random heterogeneous materials using machine learning based on artificial neural networks. For the image reconstruction, Chen et al[21] combined the autoencoder, deconvolution network and shortcut connections into the residual encoder-decoder convolutional neural network (RED-CNN) for low-dose X-ray computed tomography (CT). In[22], a direct deep learning image reconstruction method, called AUTOMAP (automated transform by manifold approximation), was proposed. Good results were reported for variously undersampled magnetic resonance imaging (MRI). For positron emission tomography (PET), a novel end-to-end PET image reconstruction technique, called DeepPET, was proposed to take the PET sinogram data as the input for quickly outputs of high quality, quantitative PET images[23]. Recently, Gao et al[24] has developed a generative adversarial network (GAN)-based deep-learning model for low-quality defect image reconstructions. The experimental results show that the proposed method has achieved great performances under different masks and noises. In the field of non-destructive testing (NDT), Piao et al[25] fused the rational Bezier curve (RBC) model with the least-square support vector machine (LS-SVM) for fast reconstruction of three-dimensional (3-D) defect profiles from three-axis magnetic flux leakage (MFL) signals. Zhang[26] et al proposed a semi-supervised probability imaging algorithm to present the damage state in aluminium plate and composite plate in the absence of damage samples. Since the limited size of datasets as the input is the major bottleneck in use of machine learning algorithms for engineering applications, a new model[27] to augment training data has been developed to estimate the size of local wall thinnings.

Inspired by the successful applications of machine learning algorithms in engineering, a novel data-driven robust framework, called Deep-guide, has been proposed for the defect reconstruction in this paper. To generate datasets for training the proposed deep learning network, a modified boundary element method (MBEM) has been developed to efficiently calculate stress and displacement fields of the scattered waves for reflection coefficients, which are used as the input signals for manifold learning to realize the end to end mapping of the transformed features to defect profiles. The proposed Deep-guide has enabled the automated learning of defect profiles throughout the homeomorphic manifold analysis and facilitate the defect representation in the spatial domain from feature extractions of reflection coefficients in the wavenumber domain with high levels of accuracy and efficiency.

2. Method

2.1 Knowledge-driven guided wave analysis for solving the inverse problem

Defect reconstruction in structures using guided waves belongs to solving an inverse problem in non-destructive testing, which can be formalized as

$$\hat{\boldsymbol{y}} = \boldsymbol{\mathcal{H}}(\boldsymbol{x}) + \boldsymbol{e} \tag{1}$$

where $\boldsymbol{\mathcal{H}}(\boldsymbol{x})$ is the mapping function to be constructed for describing the unknown defect profile $\boldsymbol{x}$ in use of the noisy signals $\hat{\boldsymbol{y}}$. The mapping $\boldsymbol{\mathcal{H}}: \boldsymbol{x} \in \mathbb{R}^D \rightarrow \hat{\boldsymbol{y}} \in \mathbb{R}^M$ is the forward operator that represents the guided wave scattering system in M dimension from the D-dimension space. $\boldsymbol{e}$ denotes the signal noise in M-dimension space and it reflects a random source of corruptions in the data $\hat{\boldsymbol{y}}$.

When the wave scattering effect is weak, $\boldsymbol{\mathcal{H}}$ can be approximately formulated as a linear operator $\boldsymbol{\mathcal{H}} \in R^{M\times D}$, and the corresponding inverse operator can be determined by

$$\boldsymbol{x} = \boldsymbol{\mathcal{H}}^{\mathrm{inv}}(\boldsymbol{y}) \tag{2}$$

where $\boldsymbol{\mathcal{H}}^{\mathrm{inv}}$ defines the mapping from M to D dimension space. It is evident that one of linear guided wave defect reconstruction methods such as wavenumber-spatial domain transform[8] has successfully achieved good quality reconstructions of $\boldsymbol{x}$ from $\boldsymbol{y}$ by a linear mapping (e.g., Fourier transform). However, the scattering would be strong in practice and problems defined in Eq.1 are often ill-posed. Taking into account these facts, the standard approach for solving such problems is to reconstruct the defects by the formulation of an iterative modelling technique, such as Quantitative detection of Fourier transform (QDFT)[12]. The above observations inspire a knowledge-driven approach, where the forward and inverse operators are determined by physical principles of the defect reconstruction process.

2.2 Manifold learning for guided wave-based defect reconstruction technique

The proposed data-driven approach in this paper, called Deep-guide, is formulated as follows:

$$\boldsymbol{x} = \boldsymbol{\mathcal{H}}^{\mathrm{net}}(\tilde{\boldsymbol{y}}\,; \hat{\boldsymbol{\theta}}) \tag{3}$$

where the operator $\boldsymbol{\mathcal{H}}^{\mathrm{Net}}$ represents a deep neural network and realizes the end-to-end mapping of the noisy scattering signal $\tilde{\boldsymbol{y}}$ to the unknown defect $\boldsymbol{x}$. $\boldsymbol{\mathcal{H}}^{\mathrm{Net}}$ is modelled by a vector of optimal parameters $\widehat{\boldsymbol{\theta}}$, which is optimized for the minimization of a loss function and also determined as follows:

$$\widehat{\boldsymbol{\theta}} = \underset{\boldsymbol{\theta}}{\operatorname{argmin}} \sum_{n=1}^{N} L_{\mathrm{net}}(\boldsymbol{\mathcal{H}}^{\mathrm{net}}(\tilde{\boldsymbol{y}}_n\,;\,\boldsymbol{\theta}); \boldsymbol{x}_n) \tag{4}$$

where $\tilde{\boldsymbol{y}}_n$ is the vector encompassing the noisy inputs and it is paired with the vector $\boldsymbol{x}_n$ of the desired outputs. It is noted that the role of the loss function L_{net} for the network is to examine the total discrepancy between the training dataset pairs for the minimization. It is also necessary that the space represented by the training data should sufficiently cover the domain of potential future inputs. Obviously, when the training session for the neural network generation is complete, the network has the capability to map a new supplied input $\tilde{\boldsymbol{y}}$ using $\boldsymbol{\mathcal{H}}^{\mathrm{net}}$ for the correct prediction of the unknown ground truth $\boldsymbol{x}$.

The schematic diagram of Deep-guide is shown in Fig. 1 for the description of manifold learning-based structural defect reconstruction using the fusion of an arbitrary guided wave scattering analysis and a paired class of defects $\boldsymbol{x} \in \mathbb{R}^D$ and noisy scattering signals $\tilde{\boldsymbol{y}} \in \mathbb{R}^M$. Based on the manifold distribution principle[28] and the geometric interpretation of deep learning[29], there are two assumptions as follows: 1) Scattering signals $\tilde{\boldsymbol{y}}$ and defects $\boldsymbol{x}$ are able to be concentrated on the low-dimensional manifold $\mathcal{P}^{\mathcal{M}}$ and $\mathcal{P}^{\mathcal{D}}$, respectively. $\mathcal{P}^{\mathcal{M}}$ is embedded in the input space $\mathcal{M} \in \mathbb{R}^M$ and $\mathcal{P}^{\mathcal{D}}$ is a subset of the output space $\mathcal{D} \in \mathbb{R}^D$; 2) The operator $\boldsymbol{\mathcal{H}}^{\mathrm{net}}$ can realize a smooth and homeomorphic mapping function between the scattering manifold $\mathcal{P}^{\mathcal{M}}$ and the reconstruction manifold $\tilde{\mathcal{P}}^{\mathcal{D}}$, where $\tilde{\mathcal{P}}^{\mathcal{D}}$ represents the approximation of $\mathcal{P}^{\mathcal{D}}$[24].

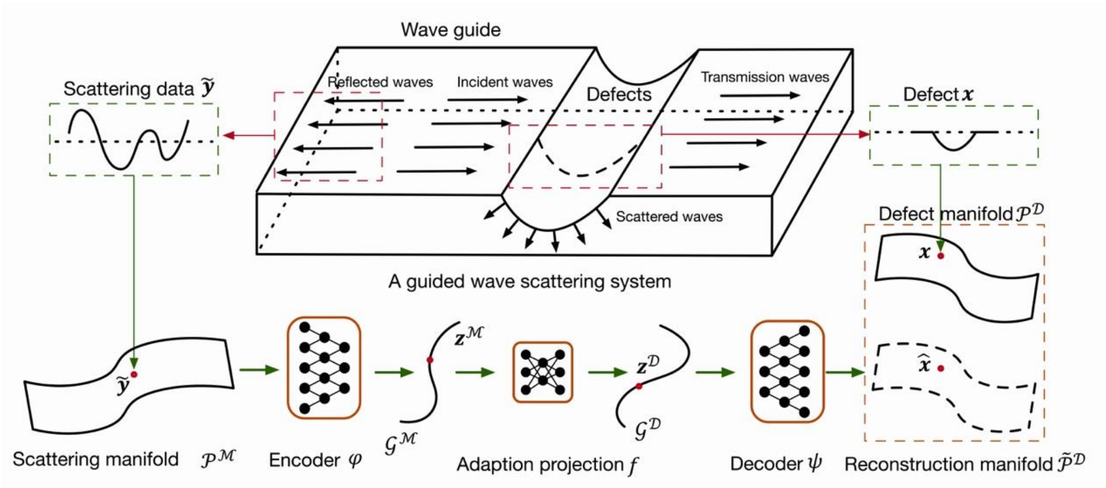

Fig. 1. The overall schematic architecture of the proposed Deep-guide for structural defect reconstruction. The deep-learning network including the encoder φ, the adaption projection f and the decoder ψ, realizes an end-to-end mapping between the scattering noise data $\tilde{\boldsymbol{y}}$ and the approximate profile of defect $\hat{\boldsymbol{x}}$. In the process of intelligent learning, the Deep-guide framework implicitly connects a scattering manifold $\mathcal{P}^{\mathcal{M}}$ from the scattering data $\tilde{\boldsymbol{y}}$ with the approximate defect manifold $\tilde{\mathcal{P}}^{\mathcal{D}}$ by realizing the reconstruction function $\hat{\boldsymbol{x}} = \psi \cdot f \cdot \varphi(\tilde{\boldsymbol{y}})$.

The neural network $\boldsymbol{\mathcal{H}}^{\mathrm{net}}$ developed in Deep-guide consists of three parts: the encoder, the latent projection and the decoder. The decomposition of the mapping function $\boldsymbol{x} = \boldsymbol{\mathcal{H}}^{\mathrm{net}}(\tilde{\boldsymbol{y}}\,;\widehat{\boldsymbol{\theta}})$ during the reconstruction process is shown in Fig. 2. First, the encoder operator φ takes a sample

$\tilde{\boldsymbol{y}} \in \mathcal{M}$ and maps it to $\boldsymbol{z}^{\mathcal{M}} \in \mathcal{F}^{\mathcal{M}}$, $\boldsymbol{z}^{\mathcal{M}} = \varphi(\tilde{\boldsymbol{y}})$, where $\boldsymbol{z}^{\mathcal{M}}$ is the latent representation of the scattering data $\tilde{\boldsymbol{y}}$. The encoder is mathematically formulated as follows:

$$\{(\mathcal{M}, \tilde{\boldsymbol{y}}), \mathcal{P}^{\mathcal{M}}\} \xrightarrow{\varphi} \{(\mathcal{F}^{\mathcal{M}}, \boldsymbol{z}^{\mathcal{M}}), \mathcal{G}^{\mathcal{M}}\} \tag{5}$$

It is noted that the role of the encoder $\varphi : \mathcal{M} \rightarrow \mathcal{F}^{\mathcal{M}}$ maps the scattering manifold $\mathcal{P}^{\mathcal{M}}$ to its latent representation $\mathcal{G}^{\mathcal{M}} = \varphi(\mathcal{P}^{\mathcal{M}})$ homeomorphically. This enables the feature extraction of the scattering data in a comparatively low-dimensional space and well capture of the main variations in the data.

Then, the adaption projection $f : \mathcal{F}^{\mathcal{M}} \rightarrow \mathcal{F}^{\mathcal{D}}$ maps $\boldsymbol{z}^{\mathcal{M}}$ to $\boldsymbol{z}^{\mathcal{D}}$ and the reduced scattering manifold $\mathcal{G}^{\mathcal{M}}$ to the adjustable manifold $\mathcal{G}^{\mathcal{D}}$, where $\mathcal{G}^{\mathcal{D}}$ is the latent representation of defect manifold $\mathcal{P}^{\mathcal{D}}$. The adaption projection realizes the inter-manifold projection and can be expressed by

$$\{(\mathcal{F}^{\mathcal{M}}, \boldsymbol{z}^{\mathcal{M}}), \mathcal{G}^{\mathcal{M}}\} \xrightarrow{f} \{(\mathcal{F}^{\mathcal{D}}, \boldsymbol{z}^{\mathcal{D}}),\ \mathcal{G}^{\mathcal{D}}\} \tag{6}$$

Following the encoder and adaption projection processes, the decoder $\psi : \mathcal{F}^{\mathcal{D}} \rightarrow \mathcal{D}$ maps $\boldsymbol{z}^{\mathcal{D}}$ to the reconstruction defect $\hat{\boldsymbol{x}}$, and creates a local parametric representation $\tilde{\mathcal{P}}^{\mathcal{D}}$ of the adjustable manifold $\mathcal{G}^{\mathcal{D}}$. $\tilde{\mathcal{P}}^{\mathcal{D}}$ approximates to the defect manifold $\mathcal{P}^{\mathcal{D}}$ and $\hat{\boldsymbol{x}}$ is similar to the ground truth $\boldsymbol{x}$. The decoder is given by

$$\{(\mathcal{F}^{\mathcal{D}}, \boldsymbol{z}^{\mathcal{D}}),\ \mathcal{G}^{\mathcal{D}}\} \xrightarrow{\psi} \{(\mathcal{D}, \hat{\boldsymbol{x}}),\ \tilde{\mathcal{P}}^{\mathcal{D}}\} \tag{7}$$

Summarily, the inverse process $\hat{\boldsymbol{x}} = \psi \cdot f \cdot \varphi(\tilde{\boldsymbol{y}})$ of guided wave defect reconstruction is achieved with the mathematical representation shown in Eq (8)

$$\{(\mathcal{M}, \tilde{\boldsymbol{y}}),\ \mathcal{P}^{\mathcal{M}}\} \xrightarrow{\varphi} \{(\mathcal{F}^{\mathcal{M}}, \boldsymbol{z}^{\mathcal{M}}), \mathcal{G}^{\mathcal{M}}\} \xrightarrow{f} \{(\mathcal{F}^{\mathcal{D}}, \boldsymbol{z}^{\mathcal{D}}),\ \mathcal{G}^{\mathcal{D}}\} \xrightarrow{\psi} \{(\mathcal{D}, \hat{\boldsymbol{x}}),\ \tilde{\mathcal{P}}^{\mathcal{D}}\} \tag{8}$$

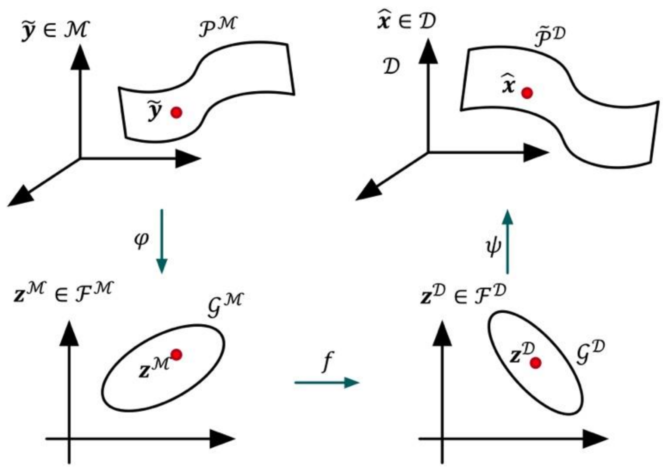

Fig. 2. The reconstruction process is decomposed into an encoding map φ, an adaption projection f and a decoding map ψ.

It is worthy of noting that the input data $\tilde{\boldsymbol{y}}$ is usually corrupted by noise and as described in denoising autoencoder[30], reconstruction of a defect using the contaminated scattering data can be inferred from the perspective of manifold learning and this indicates that the reconstruction operator $\boldsymbol{\mathcal{H}}^{\text{net}}$ in Deep-guide is robust to noise. As shown in Fig. 3, suppose that a special class of clean scattering data $\boldsymbol{y}$ is represented by a manifold $\mathcal{P}^{\mathcal{M}}$ in a low-dimensional space.

Obviously, the sample $\tilde{\boldsymbol{y}}$ with noisy contamination obtained by applying corruption process $q(\tilde{\boldsymbol{y}} \mid \boldsymbol{y})$ will locate its position away from the manifold and the crosses marked in red indicate this information. Throughout the learning process, the training stage aims at the determination of a stochastic mapping operator $p(\hat{\boldsymbol{x}} \mid \tilde{\boldsymbol{y}})$ that projects $\tilde{\boldsymbol{y}}$ onto the clean reconstruction manifold $\tilde{\mathcal{P}}^{\mathcal{D}}$, which is similar to truth defect manifold $\mathcal{P}^{\mathcal{D}}$. Fig. 4 shows that the manifold structure of a scattering data set contains 200 clean signals and 200 noisy signals (with $15\,\mathrm{dB}$ white Gaussian noise). Each signal has the dimension of 300×1, and is treated as a point in the input space $\mathcal{M} \in \mathbb{R}^{\mathbf{300}}$.

In order to perform nonlinear dimensionality reduction on high-dimensional scattering signals, this study utilizes the t-Distributed Stochastic Neighbor Embedding (t-SNE) algorithm[31] to map scattering data onto a three-dimensional space, and each sample is represented as a single point in the reduced space of manifold. As compared with other manifold learning algorithms such as LLE[32], and Isomap[33], t-SNE has advantages including its remarkable effectiveness in preserving local structure, high-quality visualization for data exploration and analysis, and computational efficiency and scalability for large-scale datasets due to the implementation of stochastic gradient descent[22].

In Fig. 4a, the clean scattering signals are depicted as the symbol 'circles' marked in blue and the noise signals are marked in red. Fig. 4b shows the manifold structure of reconstruction results generated by the operator $\boldsymbol{\mathcal{H}}^{\mathrm{net}}$ using 400 samples of defects $\hat{\boldsymbol{x}}$ with the dimension of 144×1. Results demonstrate that the proposed operator $\boldsymbol{\mathcal{H}}^{\mathrm{net}}$ in Deep-guide has the ability to remove the noise from the corrupted signals and reconstruct a clean manifold.

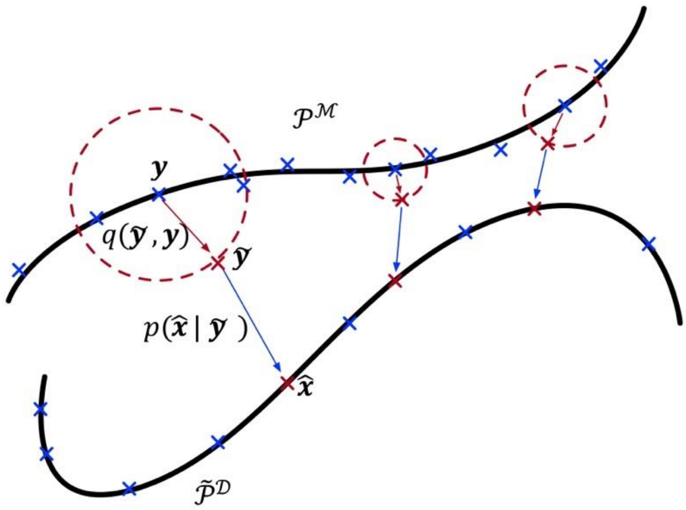

Fig. 3. From the perspective of manifold learning: Schematics of the adaptive denoising capability in defect reconstruction.

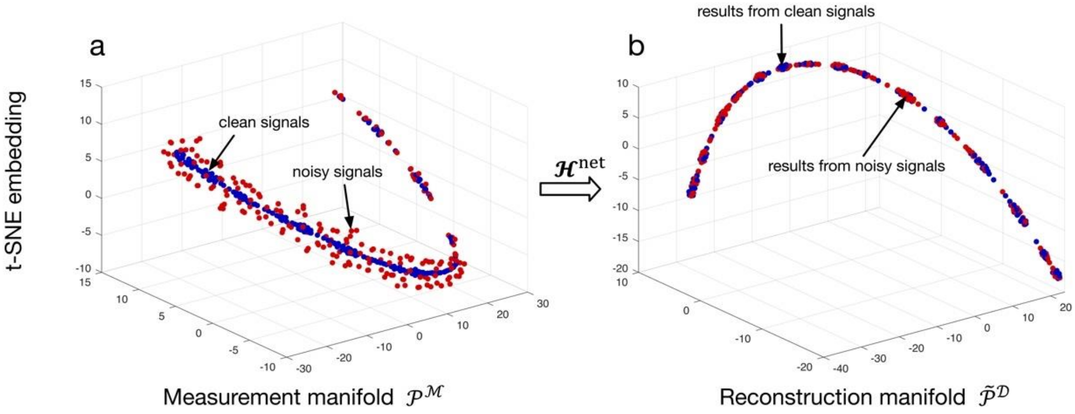

Fig. 4. Visualization of the adaptive denoising in the process of defect reconstruction using t-SNE algorithm. Results of (a) the scattering dataset and (b) the reconstructed defects in three-dimensional space.

2.3 Deep-guide network architecture

To realize the manifold learning-assisted structural defect reconstruction in Section 2.2, the proposed Deep-guide network architecture is designed to extract main features from the noisy scattering signals using three components: an encoder φ, an adaption projection f and a decoder ψ. The input data $\tilde{\boldsymbol{y}}$ to the Deep-guide network is a $2m \times 1$ real-valued vector reshaped from a $m \times 1$ complex-valued coefficients vector in frequency domain and the output $\hat{\boldsymbol{x}}$ in spatial domain is of the size $l \times 1$ ($l = 144$ in this study). As shown in Fig 5, the encoder and the decoder consist of sequential blocks of convolutional layers and the adaption projection is composed of fully connected layers. The structure of the convolutional blocks includes the convolutional filters of 3×1 with stride 1, the batch normalization (BN) and the activation function of a rectified linear unit (ReLU). The encoder contracts the input data by a max pooling layer with stride 2 and outputs 32 features in dimension of $m \times 1$. Each feature is achieved by applying a non-linear function to the input scattering data $\tilde{\boldsymbol{y}}$ and contains the useful information about the reconstruction defects. This is inspired by the mechanism of the homeomorphic mapping $\mathcal{G}^{\mathcal{M}} = \varphi(\mathcal{P}^{\mathcal{M}})$ in the manifold learning process as aforementioned. The first hidden layer in adaption projection with $l/2$ neurons is fully connected to the output layer of the encoder and activated by the hyperbolic tangent function. Then, this hidden layer is duplicated and four convolutional layers with the same parameter setting as the layers in the encoder are repeated in the decoding process. After setting upsamples, the contracted adaption representation $\boldsymbol{z}^{\mathcal{D}}$ is projected by the decoder into reconstruction defects $\hat{\boldsymbol{x}}$.

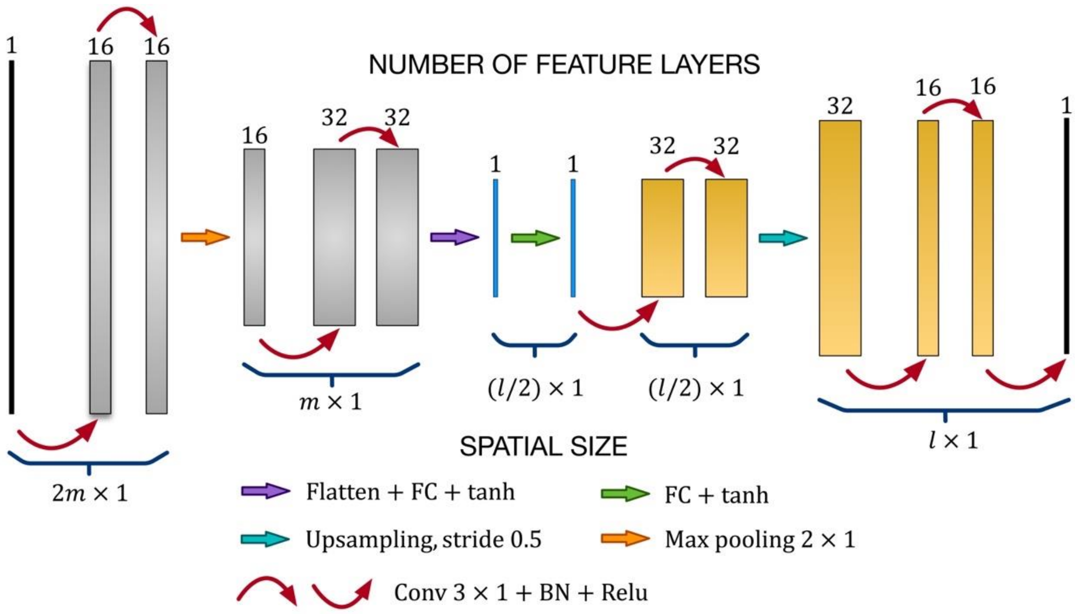

Fig. 5. The Deep-guide architecture is composed of a convolutional encoder (using a max pooling layer with stride 2 for dimensionality reduction), a two-layer fully connected adaption projection and a convolutional upsampling decoder (using fractional stride of 0.5 for upsampling by a factor of 2).

2.4 Dataset generation by guided wave analysis for solving the forward problem

In this paper, reconstruction of surface thinning flaws in a 2-dimensional steel plate using guided waves is performed, with the aid of the proposed Deep-guide framework, which is capable of quantitative defect profile sizing using different types of incident guided waves, such as SH-waves and Lamb waves.

The problem configuration is set as following: a thinning defect is localized on the upper surface of a two-dimensional plate as shown in Fig 6a, where h represents the plate thickness, w and d the width and depth of the defect, respectively. In order to simplify the problem, the plate is assumed to be infinitely large to suppress the edge reflections in modelling process. As shown by Fig. 6, S_∞^- and S_∞^+ are intact plate surfaces at left and right sides of the flaw, tending to minus and plus infinity of x_1-axis, respectively. E^- and E^+ are points where scattered waves are observed, assumed to be located on S_∞^- and S_∞^+, respectively, which are far enough from the defects. As an example, the guided Lamb wave of the nth mode is selected as the incident wave, propagating from the left side to right, and then scattered by the thinning part and the reflected and transmitted waves are observed at the far field.

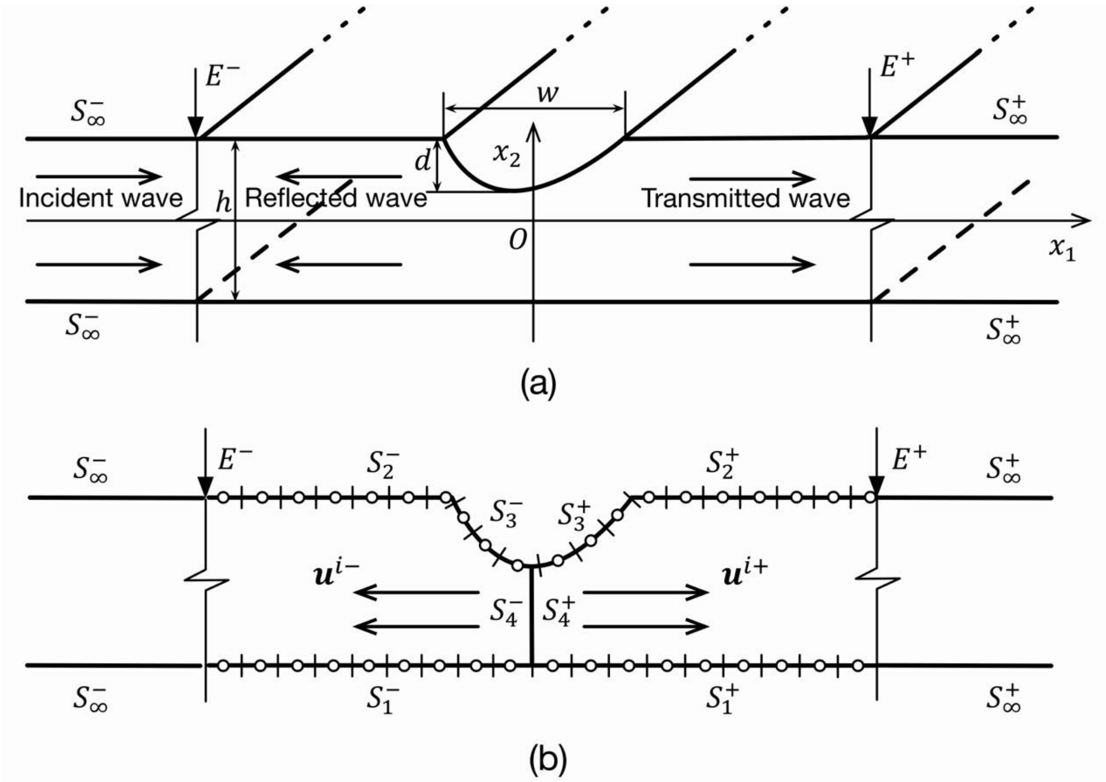

Fig. 6. Illustration of the forward analysis of the guided wave scattering problem. (a) Iso view of the guided wave scattering by a plate thinning. (b) Schematic diagram for the modified boundary element method.

According to the far-field assumption[8], the reflected and transmitted wave fields at the far field can be expressed as the summation of a series of guided Lamb wave modes:

$$\boldsymbol{u}^{\mathrm{ref}}(\boldsymbol{x},\omega) \approx R_1^-\boldsymbol{u}^{1-}(\boldsymbol{x},\omega) + R_2^-\boldsymbol{u}^{2-}(\boldsymbol{x},\omega) + \cdots + R_n^-\boldsymbol{u}^{n-}(\boldsymbol{x},\omega) \text{ where } \boldsymbol{x} \in S_\infty^- \tag{9}$$

$$\boldsymbol{u}^{\mathrm{tra}}(\boldsymbol{x},\omega) \approx R_1^+\boldsymbol{u}^{1+}(\boldsymbol{x},\omega) + R_2^+\boldsymbol{u}^{2+}(\boldsymbol{x},\omega) + \cdots + R_n^+\boldsymbol{u}^{n+}(\boldsymbol{x},\omega) \text{ where } \boldsymbol{x} \in S_\infty^+ \tag{10}$$

where the coordinate vector $\boldsymbol{x}$ is in the form of (x_1, x_2), ω is the circular frequency. $\boldsymbol{u}^{i\pm}(\boldsymbol{x},\omega)$ $(i = 1 \dots n)$ is the unit wave structure of the ith Lamb mode propagating towards positive or negative x_1 directions, respectively. $R_i^\pm(\omega)$ are the corresponding complex amplitudes and termed as transmission and reflection coefficients, respectively.

The transmission and reflection coefficients are in frequency domain, and can be obtained by FFT from time-domain data in practice[34]. To reconstruct the plate surface thinning defect, the matrix $\boldsymbol{R}^{\mathrm{ref}}$ representing multifrequency reflection coefficients is taken as the input of Deep-guide framework to reconstruct the plate' surface thinning defect. The Deep-guide neural network is mathematically formulated as

$$\boldsymbol{x} = \boldsymbol{\mathcal{H}}^{\mathrm{net}}\left(\boldsymbol{R}^{\mathrm{ref}}; \widehat{\boldsymbol{\theta}}\right) \tag{11}$$

where

$$\boldsymbol{R}^{\mathrm{ref}} = \begin{bmatrix} R_1^-(\omega_1) & \cdots & R_n^-(\omega_1) \\ \vdots & \ddots & \vdots \\ R_1^-(\omega_m) & \cdots & R_n^-(\omega_m) \end{bmatrix} \tag{12}$$

$\boldsymbol{\mathcal{H}}^{\mathrm{Net}}$ and $\widehat{\boldsymbol{\theta}}$ are defined in Eq. 3.

In order to efficiently generate sufficient data for the powerful data-mining capability of Deep-guide framework, the modified boundary element method (MBEM)[35-36] has been applied to simulate and predict reflection coefficients of guided waves propagating through thinning defects. The role of MBEM in this research not only provides the theoretical basis, but an insight to the fusion of numerical analysis and data-driven learning method for quantitative reconstruction of defects using ultrasonic guided waves in the field of nondestructive evaluation. As shown in Fig 6b, S_3 is the defect region. According to reciprocal theorem[37], the integral equation for solving the two-dimensional elastic wave scattering problem can be expressed as

$$\int_S \left[u_{\alpha\beta}^*(\boldsymbol{X},\boldsymbol{x},\omega)t_\alpha^{\mathrm{sca}}(\boldsymbol{x},\omega) - t_{\alpha\beta}^*(\boldsymbol{X},\boldsymbol{x},\omega)u_\alpha^{\mathrm{sca}}(\boldsymbol{x},\omega)\right]dS(\boldsymbol{x}) = \frac{1}{2}u_\alpha^{\mathrm{sca}}(\boldsymbol{X},\omega) \quad \alpha,\beta = 1,2 \quad \boldsymbol{X} \in S_1 \cup S_2 \cup S_3 \tag{13}$$

where $\boldsymbol{X}$ and $\boldsymbol{x}$ are the source and field points, respectively. ω is the circular frequency; S_3 defines the flaw region; S_1 and S_2 are free-traction surfaces. $u_\alpha^{\mathrm{sca}}(\boldsymbol{X},\omega)$ and $t_\alpha^{\mathrm{sca}}(\boldsymbol{x},\omega)$ denote displacements and stresses of the scattering wave. $u_{\alpha\beta}^*(\boldsymbol{X},\boldsymbol{x},\omega)$ and $t_{\alpha\beta}^*(\boldsymbol{X},\boldsymbol{x},\omega)$ represent the full-space Green's function of displacements and stresses. Since $u_\alpha^{\mathrm{sca}}(\boldsymbol{x},\omega)$ at the infinite boundary can be expressed in the form of Eqs. 9 and10, the integral term at the infinite boundary in Eq. 13 can be reformulated as follows:

$$\int_{S_\infty^\pm} t_{\alpha\beta}^*(\boldsymbol{X},\boldsymbol{x},\omega)u_\alpha(\boldsymbol{x},\omega)\, dS(\boldsymbol{x}) = \sum_{i=1}^{n} R_i^\pm(\omega)A_i^\pm(\boldsymbol{X}) = \sum_{i=1}^{n} R_i^\pm(\omega)\int_{S_\infty^\pm} t_{\alpha\beta}^*(\boldsymbol{X},\boldsymbol{x},\omega)u_\alpha^{i\pm}(\boldsymbol{x},\omega)\, dS(\boldsymbol{x}) \tag{14}$$

where $R_i^\pm(\omega)$ is the scattering coefficient, $A_i^\pm(\boldsymbol{X})$ is defined as the modified item. Traditional boundary element method ignores the integral term at the infinite boundary, which leads to the spurious perturbation by reflected waves at the artificially truncated sections. In order to eliminate such influence and calculate the integral term, a fictitious boundary S_4 is introduced to divide the whole boundaries into two regions shown in Fig. 6b. Applying a reciprocal identity method between a unit Lamb mode and the Green's function with the source at $\boldsymbol{X}$ to the half infinite plate bounded by $S_\infty^\pm$, the modified item $A_i^\pm(\boldsymbol{X})$ can also be expressed as

$$\begin{aligned} A_i^\pm(\boldsymbol{X}) &= -\frac{1}{2}u_\alpha^{\mathrm{inc}}(\boldsymbol{X},\omega) - \int_{S_1^\pm+S_2^\pm+S_3^\pm+S_4^\pm} t_{\alpha\beta}^*(\boldsymbol{X},\boldsymbol{x},\omega)u_\alpha^\pm(\boldsymbol{x},\omega)dS(\boldsymbol{x}) \\ &+ \int_{S_1^\pm+S_2^\pm+S_3^\pm+S_4^\pm} u_{\alpha\beta}^*(\boldsymbol{X},\boldsymbol{x},\omega)t_\alpha^\pm(\boldsymbol{x},\omega)dS(\boldsymbol{x}) \quad \alpha,\beta = 1,2 \quad \boldsymbol{X} \in S_1 \cup S_2 \cup S_3 \quad \boldsymbol{x} \in S_1 \cup S_2 \cup S_3 \cup S_4 \end{aligned} \tag{15}$$

Substituting Eq.15 into Eq.14, the discretized Eq. 13 can be rewritten as

$$\sum_{e\in S_1\cup S_2\cup S_3}\sum_{\eta=1}^{N_e} \boldsymbol{T}_{\gamma\eta}\cdot \boldsymbol{u}(\boldsymbol{x}_\eta,\omega) + \sum_{i=1}^{n}\left[R_i^- A_i^-(\boldsymbol{X}_\gamma) + R_i^+ A_i^+(\boldsymbol{X}_\gamma,\omega)\right] = \sum_{e\in S_1\cup S_2}\sum_{\eta=1}^{N_e} \boldsymbol{G}_{\gamma\eta}\cdot \boldsymbol{t}(\boldsymbol{x}_\eta,\omega) \tag{16}$$

where N_e is the number of the discrete elements; $\boldsymbol{T}_{\gamma\eta}$ and $\boldsymbol{G}_{\gamma\eta}$ are the fundamental solutions matrixes of the local element. After assembling all element matrixes, the global equilibrium equation can be established as follows:

$$\boldsymbol{H}\cdot\boldsymbol{U} + \boldsymbol{A}\cdot\boldsymbol{R} = \boldsymbol{G}\cdot\boldsymbol{T} \tag{17}$$

where global matrixes $\boldsymbol{H}$, $\boldsymbol{G}$, $\boldsymbol{U}$, $\boldsymbol{T}$, $\boldsymbol{A}$ and $\boldsymbol{R}$ are obtained by assembling $\boldsymbol{T}_{\gamma\eta}$, $\boldsymbol{G}_{\gamma\eta}$, the node displacement $\boldsymbol{u}(\boldsymbol{x}_\eta,\omega)$, the node traction $\boldsymbol{t}(\boldsymbol{x}_\eta,\omega)$, the correction $A_i^\pm(\boldsymbol{X})$ and the scattering coefficients $R_i^\pm$, respectively.

Then, the acoustic signals of scattering coefficients are obtained by solving the Eq. 17. Based on the information for defect reconstruction using manifold learning described in Sections 2.2-2.4, the framework of the proposed Deep-guide can be illustrated in Algorithms 1 below.

Algorithm 1: The manifold-learning assisted Deep-guide framework

input :

- $\boldsymbol{x}$: The original ground truth defect datasets
- $\boldsymbol{R}^{\text{uk}}$: The reflection coefficients of an unknown defects
- h, E, ν, ρ : The parameters of structure : thickness, Young modulus, Poisson coefficient, density
- $d^{\text{grid}}, d^{\text{tru}}$ The parameters of numerical calculation: size of the element, distance of truncation
- $\alpha, \epsilon, t, m_0, v_0, \beta_1, \beta_2$: The parameters of stochastic optimization:

output:

- $\hat{\boldsymbol{x}}$ The reconstructed defects

▷ Build a waveguide model
Model $\leftarrow h, E, \nu, \rho$
for $\boldsymbol{x}_i$ *in* $[\boldsymbol{x}_1, \boldsymbol{x}_2, \ldots, \boldsymbol{x}_N]$ **do**
    ▷ Use MBEM to calculate the reflection coefficients $\boldsymbol{R}_i^{\text{ref}}$of the defect $\boldsymbol{x}_i$
    $\boldsymbol{R}_i^{\text{ref}} \leftarrow \text{MBEM}(\boldsymbol{x}_i, \text{Model}, d^{grid}, d^{tru})$
    ▷ Corrupt the reflection coefficients $\hat{\boldsymbol{R}}_i^{\text{ref}}$ by an additive noise
    $\hat{\boldsymbol{R}}_i^{\text{ref}} \sim q(\hat{\boldsymbol{R}}_i^{\text{ref}} \mid \boldsymbol{R}_i^{\text{ref}})$
end
▷Divide the data into training sets and test sets
$\hat{\boldsymbol{R}}^{\text{tra}}, \hat{\boldsymbol{R}}^{\text{test}} \leftarrow$ Divide $\hat{\boldsymbol{R}}^{\text{ref}}$
$\boldsymbol{x}^{\text{tra}}, \boldsymbol{x}^{\text{test}} \leftarrow$ Divide $\boldsymbol{x}$
while *Low-performance on the test set* **do**
    ▷Update the hyper-parameters of the Encoder ϕ,adaption projection f and the decoder ψ
    $\phi, f, \psi \leftarrow$ Update the hyper-parameters
    ▷Construct and initialize the neural network $H_{\theta_0}^{\text{net}}$
    $H_{\theta_0}^{\text{net}} \leftarrow \psi \cdot f \cdot \phi$
    ▷ Network training
    while θ_t not converged **do**
        $t \leftarrow t + 1$
        ▷Get gradients w.r.t. stochastic objective at timestep t
        $g_t \leftarrow \triangledown_\theta L_{\text{net}}(H_{\theta_{t-1}}^{\text{net}}(\hat{\boldsymbol{R}}^{\text{tra}}); \boldsymbol{x}^{\text{tra}})$
        ▷Compute bias-corrected first moment estimate
        $\hat{m}_t \leftarrow (\beta_1 \cdot m_{t-1} + (1 - \beta_1) \cdot g_t)/(1 - \beta_1^t)$
        ▷Compute bias-corrected second raw moment estimate
        $\hat{v}_t \leftarrow (\beta_2 \cdot v_{t-1} + (1 - \beta_2) \cdot g_t^2)/(1 - \beta_2^t)$
        ▷Update parameters
        $\theta_t \leftarrow \theta_{t-1} - \alpha \cdot \hat{m}_t/(\sqrt{\hat{v}_t} + \epsilon)$
    end
    ▷Validate the neural network on the test set
    $\boldsymbol{x}^{\text{test}} \longleftrightarrow H_{\theta_t}^{\text{net}}(\hat{\boldsymbol{R}}^{\text{test}})$
end
1
▷ Reconstruct the unknown defects
$\hat{\boldsymbol{x}} \leftarrow H_{\theta_t}^{\text{net}}(\hat{\boldsymbol{R}}^{\text{uk}})$

In the following study, material properties of the steel plate include Young modulus $E = 207.18\,\text{Gpa}$, Poisson coefficient $\upsilon = 0.2949$, the density $\rho = 7800\,\text{kg/m}^3$ and the plate thickness of $1\,\text{mm}$. The distance between two observation points E^- and E^+ is $8\,\text{mm}$ and the size of element is $0.02\,\text{mm}$, which ensures the results of MBEM with a high level of accuracy. A dataset of 4096 noisy scattering signals from three common shapes of plate surface defects, i.e. rectangular, V-notch and Gaussian-curved flaws, have been obtained by MBEM. The original defect parameters and profiles are shown in Table 1 and Fig 7. The plate thickness in all cases is $h = 1\,mm$.

Table 1 Parameters for three types of defects

	Maximum width w_{max} (mm)	Minimum width w_{min} (mm)	Maximum depth d_{max} (mm)	Minimum depth d_{min} (mm)
Rectangular defects	0.8	0.2	0.7	0.1
V-notch defects	0.8	0.2	0.7	0.1
Gaussian-curved defects	1.14	0.1	0.7	0.1

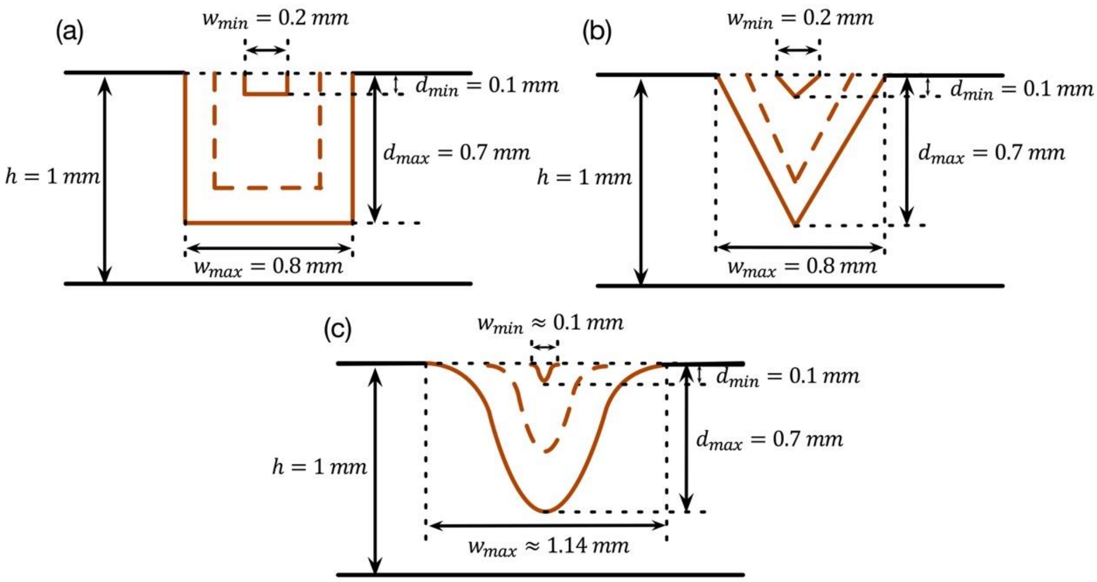

Fig. 7. Illustration of three types of defect profiles: (a) Rectangular defects, (b) V-notch defects, (c) Gaussian-curved defects (maximum variance $v_{max} = 0.2$, minimum variance $v_{min} = 0.02$).

The simulated 4096 signals have been calculated for the inputs of reflection coefficients regarding each defect. To demonstrate the robustness of the proposed Deep-guide network, all simulation results are corrupted by white Gaussian noise with the signal-to-noise ratio (SNR) randomly distributed between $5\,dB$ and $20\,dB$. Also, the original 4096 plate thinning defects have been treated as the ground truth.

Among 4096 signals, 1024 samplings were obtained from the scattering analysis of three aforementioned types of defects using the incident S_0 Lamb wave mode. For each defect, the circular frequency ω of the incident wave is ranged from 0.1 MHz to 4.0 MHz with the increment of 0.1, a total of 40 frequency samples. The amplitude coefficients of first seven Lamb wave modes have been used for the calculations at each frequency sample. Thus, the reflection coefficients of Lamb waves $\boldsymbol{R}^{\text{Lamb}}$ can be expressed as follows:

$$\boldsymbol{R}^{\text{Lamb}} = \begin{bmatrix} R_1^-(\omega_1) & \cdots & R_7^-(\omega_1) \\ \vdots & \ddots & \vdots \\ R_1^-(\omega_{40}) & \cdots & R_7^-(\omega_{40}) \end{bmatrix} \tag{18}$$

The remaining 3072 signals were obtained from the analysis using the incident 0th SH-mode. The circular frequency ω in the range of 0.1 MHz to 15.0 MHz with the increment of 0.1, includes a total of 150 frequency samples. The amplitude coefficients of the first ten SH-wave modes have been used for the calculations at each frequency sample. Therefore, the reflection coefficients of SH-waves $\boldsymbol{R}^{\text{SH}}$ can be expressed as follows:

$$\boldsymbol{R}^{\mathrm{SH}} = \begin{bmatrix} R_1^-(\omega_1) & \cdots & R_{10}^-(\omega_1) \\ \vdots & \ddots & \vdots \\ R_1^-(\omega_{150}) & \cdots & R_{10}^-(\omega_{150}) \end{bmatrix} \tag{19}$$

It is worth nothing that when Deep-guide is used for defect reconstruction, only a small number of frequency samples are required for the high-quality reconstruction. Numerical validations below will provide a reference to the number of frequency samples (F^{ref}) for practical applications of Deep-guide.

2.5 Defect quality evaluation

To quantitatively evaluate the quality of the reconstructed defects, two metrics have been used. The first criterion is the root mean square error (RMSE) formulated as:

$$\mathrm{RMSE} = \sqrt{\frac{\sum_{i=1}^{N}(x_i - \hat{x}_i)^2}{N}} \tag{20}$$

where N is the number of sampling points to represent defects, x_i is ground value of the truth defect and $\hat{x}_i$ is prediction value of the reconstructed defect.

The second metrics used for the defect quality evaluation is the peak signal-to-noise ratio (PSNR) as follows:

$$\mathrm{PSNR} = 20 \cdot \log_{10}\left(\frac{x_{\max}}{\mathrm{RMSE}}\right) \tag{21}$$

where $x_{\max}$ is the maximal value of the ground truth defects $\boldsymbol{x}$. A higher value of PSNR represents the better defect quality.

3. Numerical Validation

3.1 Validation of the proposed Deep-guide framework

To develop the Deep-guide framework with better generality for efficiently solving the inverse problem of defect reconstructions, the deep neural network model $\boldsymbol{\mathcal{H}}^{\mathrm{net}}$ has been trained using the first three modes of SH-waves and Lamb waves scattering signals, respectively. Following that, the unknown defects in the test set have been reconstructed. It is worth noting that the same network architecture and hyperparameters have been kept intact during the process of defect reconstructions whilst using two different input and output signals to evaluate the generality of the develop network. Reconstructions of defects with three types of profiles (Rectangular, V-notch and Gaussian-curved defects) using different modes of SH-waves and Lamb waves have been shown in Fig.8. The number of test samples ($N = 450$) in this research has been used. The state-of-art conventional knowledge-driven reconstruction method, which is called Born approximation-based Fourier transform (BFT)[8, 9] has been compared against the proposed method. The BFT is used to reconstruct defects using SH0 and S0 mode. It is noted that the Deep-guide framework takes less than 0.1 seconds for defect reconstruction as it only requires one pass to execute calculations. It can be observed that main features of the defects have been successfully reconstructed in all cases, where the remarkable capability of Deep-guide for defect reconstruction using different guided waves have been demonstrated.

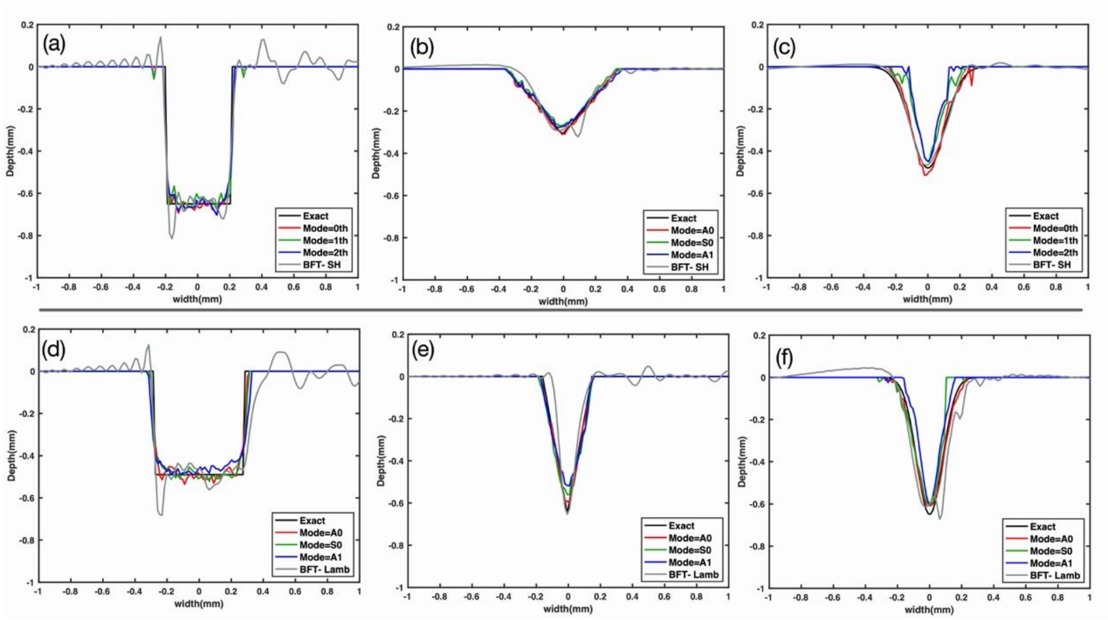

Fig.8. Reconstruction results of plate surface defects using Deep-guide framework. Plate thickness $h = 1mm$, w and d are the width and depth of the defects, respectively. Each model has been trained by 1024 sampling data with 40 circular frequency samples. Reconstructed defects with various widths and depths using (a-c) SH-wave modes and (d-f) Lamb wave modes. The yellow lines represent the reconstruction results using BFT with SH0 and S0, respectively.

Furthermore, the quantitative evaluations on the qualities of reconstruction, i.e., average RMSE and PSNR in the test set have been provided in Tables 2 and 3. For defect reconstructions by the $0th$ mode of SH-waves, the average RMSE is 0.0257, which is the lowest value as compared with results by the other two modes and BFT. Employing the developed Deep-guide framework for defect reconstruction, the result quality obtained by the $0th$ mode of SH-waves has been improved by 7% from 0.0275 of the first mode, 16.34% from 0.0299 of the second mode and 69.7% from 0.0435 of the BFT, respectively. The same conclusion can be drawn by the average PSNR - the best result is 25.3999 dB by the $0th$ mode, whilst 24.6997 dB is observed for the first mode, 23.6665 dB for the second mode and 21.2297 dB for the BFT. Overall, the best precision of defect reconstructions using the Deep-guide framework can be achieved by the $0th$ mode in first two cases. For Case 3, the result by the BFT is slightly better than defect reconstruction by the Deep-guide, this might owe to the fact that the Fourier method is more suitable for reconstructing smooth circular defects. It has been anticipated that the $0th$ mode would have the ability to reconstruct defects with complex profiles when the number of training data is increased. For the simple defect profile in Case 2, the highest accuracy of reconstruction of V-notch defects has been indicated by the RMSE value of 0.0133 obtained by the $0th$ mode of SH-waves. It has been observed that the average reconstruction performances using SH-waves can be evaluated by RMSE and PSNR over the entire test set with the values of 0.0277 and 24.5887 dB, respectively.

Furthermore, the same Deep-guide architecture has been applied for reconstruction of defects using Lamb waves. In Table 3, the smallest average RMSE (0.0262) of reconstructions by A0 Lamb wave mode in three cases has been observed, as compared with 0.0333 by the S0 mode (27.1% higher), 0.0442 by A1 mode (68.7% higher) and 0.0444 by BFT (69.5% higher).

Similarly, the quality of defect reconstructions evaluated by the average PSNR value has been also provided to demonstrate the more accuracy of results by the A0 Lamb wave mode than those by the other two modes. Again, V-notch defect reconstruction using Lamb waves has the best precision with the average RMSE (0.027), which is improved by 31.85% and 52.22% from 0.0356 and 0.0411 in Case 3 and 1, respectively. It is worth noting that the largest PSNR value of Gaussian-curved defect reconstructions by three Lamb wave modes is 25.0783 dB (A0 mode), which indicates that the developed Deep-guide framework has the capability to reconstruct the defect with a complex profile. This has well agreed with the observation from the aforementioned reconstruction by SH-waves. Also, the average RMSE over the entire test set using Lamb waves is 0.0346, which is increased by 24.91% from 0.0277 in Table 2 using SH-waves, and PSNR is decreased from 24.5887 dB to 23.6607 dB, accordingly.

In summary, the quantitative evaluation on the quality of defect reconstructions by the proposed Deep-guide framework shows that: 1) Based on the results from entire test samples, the reconstruction accuracy of the Deep-guide method is higher than that of BFT. Moreover, the results of Deep-guide have noise-free waveform in non-defective regions, which is more favorable for defect localization. 2)The reconstruction by the lower order modes performs better using either SH-waves or Lamb waves; 2) Constructing different types of defects has different reconstruction precisions in terms of RMSE and PSNR. Also, the highest reconstruction precision can be observed for V-notch defect construction by SH-waves and Lamb waves. This can be interpreted from the perspective of manifold structure illustrated in Section 3) The precision of defect reconstruction using SH-waves (24.5887 dB) is improved by 0.928 dB from the result (23.6607 dB) using Lamb waves.

Table 2 RMSE and PSNR of reconstructed defect shapes using SH-waves

		0*th* Mode	First Mode	Second Mode	Average	BFT
Case 1	RMSE	0.0255	0.0257	0.036	0.029	0.0566
Rectangular defect	PSNR(dB)	23.3692	22.9625	20.3295	22.2204	19.1993
Case 2	RMSE	0.0133	0.0136	0.0158	0.0142	0.0532
V-notch defect	PSNR(dB)	29.677	29.2967	28.0829	29.0189	19.7635
Case 3	RMSE	0.0384	0.0432	0.0379	0.0398	0.0207
Gaussian-curved defect	PSNR(dB)	23.1535	21.8398	22.5871	22.5268	24.7263
Average	RMSE	0.0257	0.0275	0.0299	0.0277	0.0435
	PSNR(dB)	25.3999	24.6997	23.6665	24.5887	21.2297

Table 3 RMSE and PSNR of reconstructed defect shapes using Lamb waves

		Mode = A0	Mode = S0	Mode = A1	Average	BFT
Case 1	RMSE	0.0345	0.0366	0.0522	0.0411	0.0586
Rectangular defect	PSNR(dB)	23.0504	22.5365	19.4565	21.6811	18.8543
Case 2	RMSE	0.0176	0.0254	0.0379	0.027	0.0492
V-notch defect	PSNR(dB)	27.0774	25.0693	22.7761	24.9743	21.6754
Case 3	RMSE	0.0266	0.0379	0.0424	0.0356	0.0245
Gaussian-curved defect	PSNR(dB)	25.0783	24.2307	23.6713	24.3268	24.8053

Average	RMSE	0.0262	0.0333	0.0442	0.0346	0.0444
	PSNR(dB)	25.0687	23.9455	21.968	23.6607	21.7783

3.2 Verification of defect localization of the Deep-guide framework

As the reflection coefficients (the input of the Deep guide framework) are complex numbers in nature, their phase information actually reflects the defect's position extracted by Deep guide network for defect localization. Fig. 9 has shown the reconstruction results by some representative methods such as QDFT[38] and BFT-SH[8] for double rectangular defects located at different positions along the width direction, demonstrating that the Deep-guide method has achieved the highest accuracy of defect localization. It has been noted that due to the periodicity of the wave field, defect localization can only be conducted in the vicinity of the defect area. Therefore, in practical inspection defect localization technique needs to consider the reception time of the wave signal: First, the defect's area is estimated based on the arrival time of the reflected wave and the wave speed, and then the precise localization is achieved by leveraging the phase information.

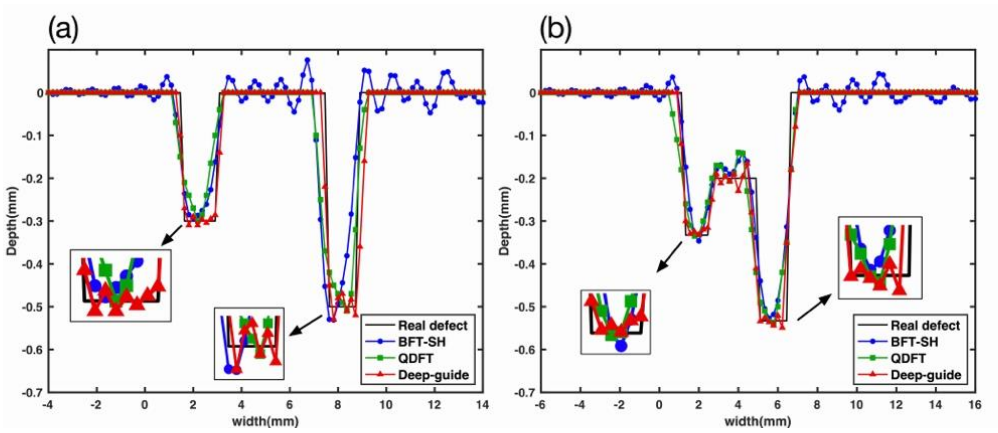

Fig. 9. Reconstruction results of two rectangular defects located at different positions.

It has been noted that the Deep-guide method has two advantages over the BFT and QDFT methods. Firstly, due to the complexity of guided wave scattering fields, BFT and QDFT methods can only construct approximate linear reconstruction models using Born approximation. While the Deep-guide method can achieve higher accuracy in reconstruction by the implementation of complex nonlinear mappings between scattering data and defect shapes; Secondly, for reconstructions by different types of guided waves or waveguides with different structures using BFT and QDFT methods, the derivation of analytical formulations and a time-consuming modelling process are required. On the contrary, the Deep-guide method has good universality and can be easily applied to different types of waveguides and defects. As the Deep-guide requires a large amount of sampling data as the input, it is challenging to achieve high-accuracy defect reconstructions using limited data. Therefore, further research studies are suggested to address this issue for the wide application of Deep-guide method in the fields of structural health monitoring and structural integrity.

3.3 Verification of 3D defect reconstruction of the Deep-guide framework

To validate the feasibility of the proposed method in solving 3D defect reconstructions, numerical experiments have been conducted to demonstrate the advantages of Deep-guide method. Technically, the 2D convolutional layer has been adopted to output the depth information of the defect in the decoder module. Furthermore, to characterize the defect dimensions including the length, width and depth within the structure, the 3D convolutional layer enables the point cloud outputs to represent the complete defect information. With these implementations, the trained Deep-guide framework by 3D guided wave scattering data has the ability to reconstruct 3D defects including the cross-section and length information.

Using the dimensionless parameters defined in Section 2.4, a surface defect in an infinitely plate with a thickness of $2h$ in Fig.10(a) has been studied. The incident S0 mode of Lamb waves along the x_1 direction has been exerted and further scattered upon encountering the defect to form a scattered wave field. 30 receivers around the defect have been placed in a circle to record the scattered wave signals. Three types of defects including the frustum, rectangular prism, and circular-rectangle combinations have been considered for reconstruction. 50 sample data for each type of defect have been used for defect reconstructions. The dimensionless frequency of scattered wave has been uniformly sampled in the range of $0.05\ to\ 0.1$ with an increment of 0.01. In this numerical experiment, FEM has been used to simulate the scattered wave field of the defects shown in Fig. 10(b). The Deep guide framework with the implementation of a 2D convolutional layer as the Decoder has been adopted for defect depth reconstruction. The contour values by the neural network have represented the depth of the defect at each of 50 sampling points. Reconstruction results have been shown in Figs. 11-13 to represent three types of defects, respectively. It has been observed that the Deep-guide method has successfully realized three-dimensional defect reconstructions, simultaneously characterizing the length, width, and depth of the defects with high accuracy as compared with the ground values.

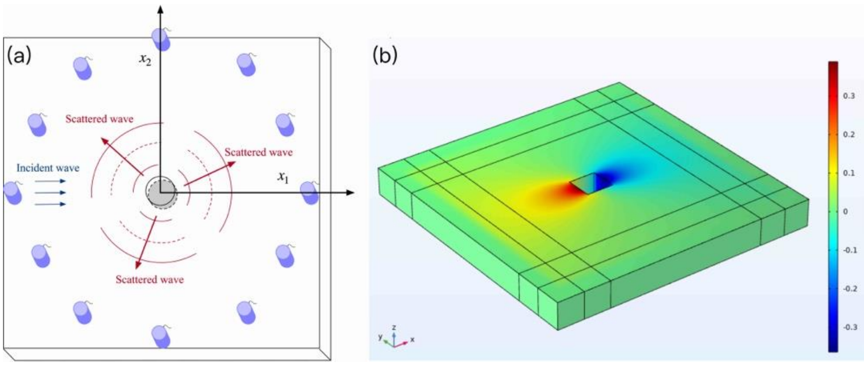

Fig. 10. (a) Scattering of incident Lamb wave on defect, received by array sensors (b) Scattering wave field simulated by FEM.

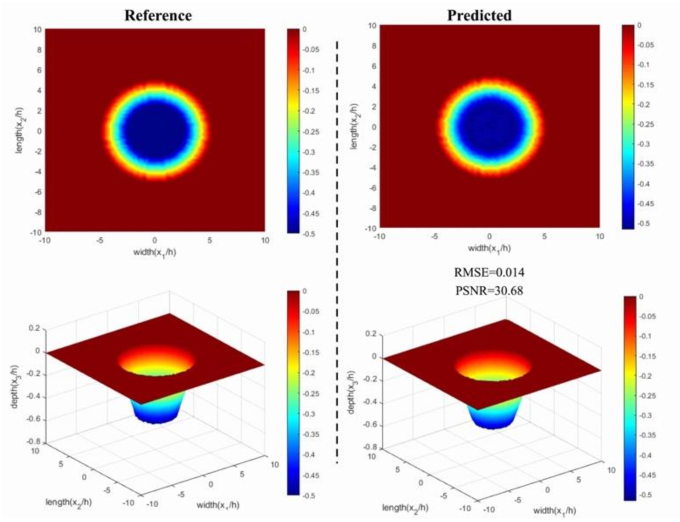

Fig. 11. Reconstruction results of a conical-shaped defect, presented in top view and 3D Iso-view in the xy plane.

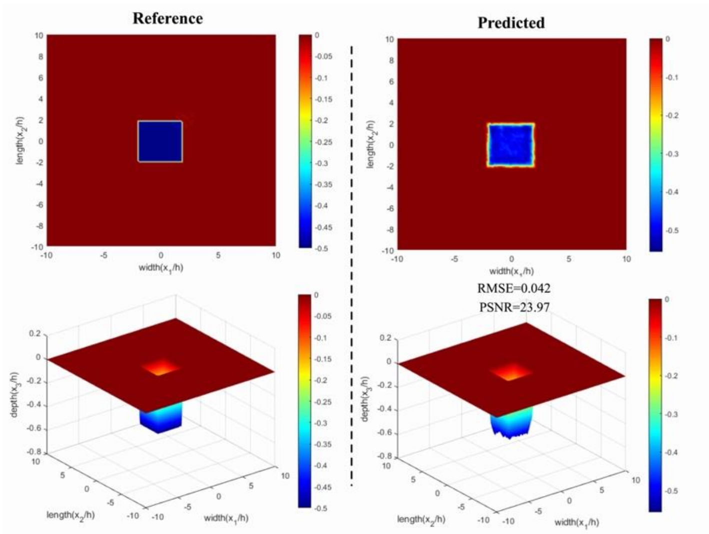

Fig. 12. Reconstruction results of a rectangular-shaped defect, shown in top view and 3D Iso-view in the xy plane.

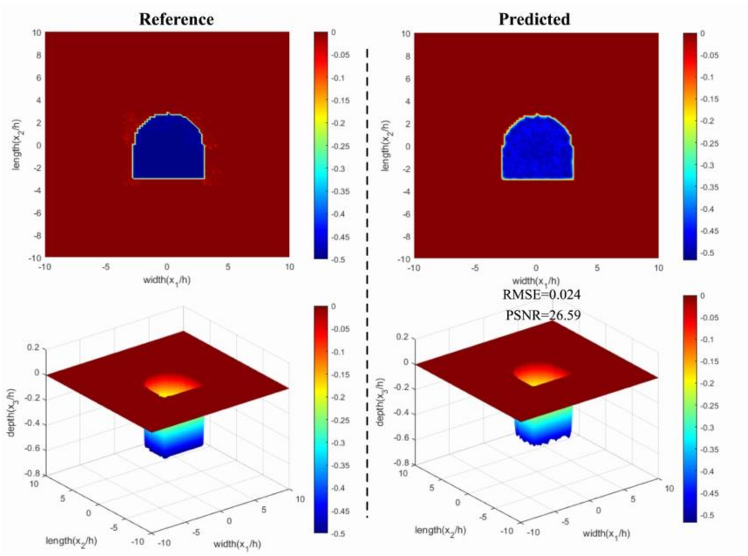

Fig. 13. Reconstruction results of a combined defect with circular and rectangular shapes, presented in top view and 3D Iso-view in the xy plane.

3.4 Effect of the number of frequency samples on the accuracy of reconstruction

As described in Section 2.4, each item in the matrix of reflection coefficients $\boldsymbol{R}^{\mathrm{ref}}$ used to reconstruct defects represents the complex amplitude of the wave mode at different circular frequency. In practice, the process of defect reconstruction by fewer frequency samples means less computational and experimental cost. However, quantitatively defect reconstruction using existing knowledge-driven methods such as the wavenumber-spatial domain transform requires at least 150 frequency samples[8]. Taking into account this situation, the effects of the number of frequency samples on the accuracy and efficiency of defect reconstruction using the 0th mode of SH-waves have been investigated in this section. To demonstrate the more superior performance of the proposed Deep-guide framework over the traditional methods for defect reconstruction, the maximal number of frequency samples used for defect reconstruction has been set to 100.

A General Case Study

First, the Deep-guide models have been trained using reflection coefficients $\boldsymbol{R}^{\mathrm{ref}}$ with different numbers of frequency samples. For a general scenario, a 450-sample dataset including three types of defects (Rectangular, V-notch and Gaussian-curved defects) has been applied to evaluate the capability of Deep-guide models for reconstructions of unknown defects in term of the accuracy. The test results show that in this general case, models generated with more frequency samples achieve better reconstruction performance, which is indicated by a relatively lower and narrower distribution of RMSE over the test dataset in Fig. 14a, whereas models trained by fewer frequency samples have poor predictions on defect reconstruction with a higher and wider range of RMSE. Also, it has been observed that the median value (0.018) of RMSE and the median value (24.285 dB) of PSNR have demonstrated that the model created by Deep-guide architecture with the input of 100 frequency samples has best prediction accuracy and superiority than other models, for example, the model by 40 frequency samples for defect reconstruction with RMSE of 0.026 (44.44% higher) and PSNR of 22.426 dB (1.859 dB lower). It has been noted that the model trained with only one frequency sample is still able to predict the defect reconstruction, however, the qualify is an issue due to results of the highest

RMSE (0.0732) and the lowest PSNR (14.0618 dB). Also, the boxplots show that when the number of frequency samples is more than 20, the reconstruction performance is relatively superior and stable as the number of frequency samples increases, while the reconstruction precision decreases rapidly when the number of frequency samples is less than 20. Therefore, the reference number of frequency samples ($F^{\mathrm{ref}} = 20$) is suggested in such condition. Furthermore, to demonstrate the effect of the number of frequency samples on the accuracy of defect reconstruction from manifold space point of view, manifold structures for input datasets with 40 frequency samples and 5 frequency samples have been visualized by t-SNE, respectively. As shown in Figs. 14c and d, the manifold structure of the 40 frequency samples dataset appears highly separable, as compared to the result by 5 frequency samples dataset. Indeed, the model trained with 40 frequency samples dataset performs better. Besides, it is worth noting that the green dots in Fig. 14c representing the manifold of the V-notch defects show higher separable, as compare with the manifolds of the other two types of defects. This interprets why the reconstruction of the V-notch defects can achieve the better accuracy shown in Section 3.1.

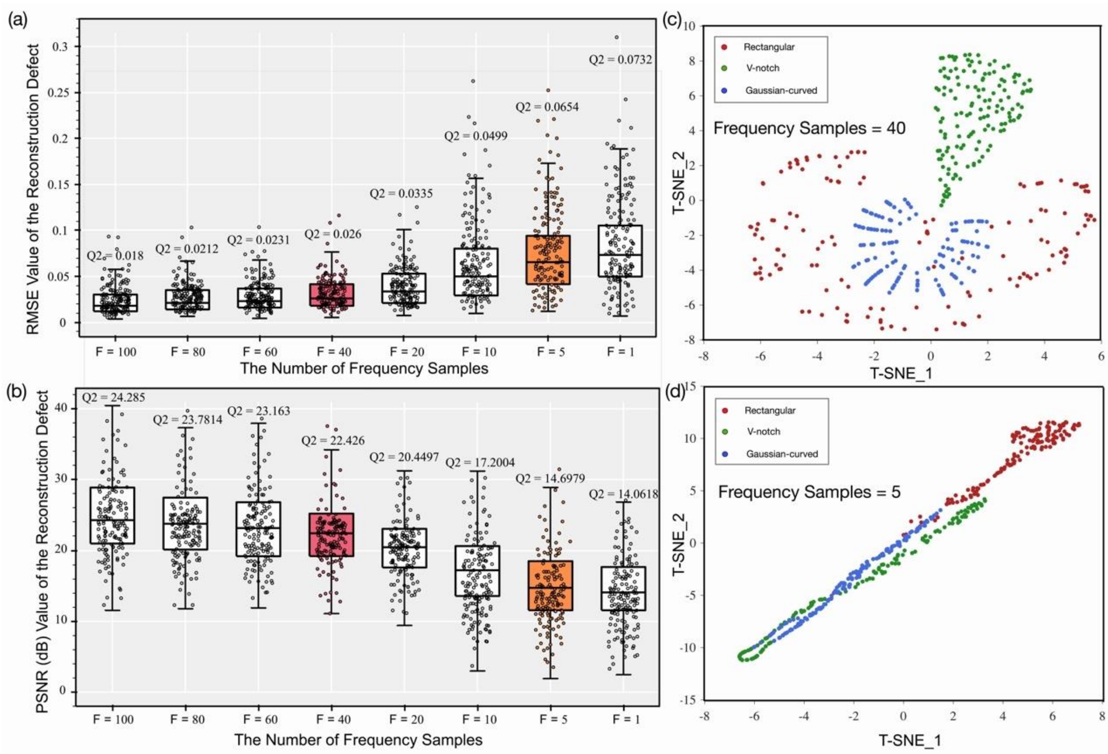

Fig. 14. Analysis of defect reconstruction with different numbers of frequency samples. (a) Quantitative evaluations on the quality of reconstruction with RMSE over the entire 450 test data. The x axis represents the number of frequency samples used for training the Deep-guide models. The y axis denotes the values of RMSE between the reconstructed defects and the ground truth. Each box shows the interquartile range (IQR between Q1 and Q3) of the training data. The central mark (the horizontal line in each box) shows the median value. The upper whisker extends from the hinge to the largest value no further than Q3+1.5×IQR and the lower whisker extends from the hinge to the smallest value at most Q1−1.5×IQR. For each box, 150 values randomly selected from the 450 test results are shown as dots. (b) Quantitative evaluations on the quality of reconstruction with PSNR over the entire 450 test set. (c) Visualization of manifold structures of the input dataset with 40 frequency samples and (d) 5 frequency samples, respectively.

A Special Case Study

Usually, a high-accuracy detection and reconstruction for a particular flaw or defect is required in some areas such as railway transportation, oil pipelines and aerospace so that structural integrity can be quantitatively evaluated and assessed for the prediction of its remaining service life. Take into account this situation, a specific case for defect reconstruction has been investigated in this section. As the methodology applied to the above general scenario, 350 unknown Gaussian-curved defects have been used as training data to reconstruct this representative defect. The quantitative evaluations on the qualities of reconstruction, i.e., boxplots of the RMSE and PSNR over the entire test set have been provided in Figs. 15a and b. As the number of frequency samples increases, the trained neural network model has better predictions on defect reconstruction with a lower and narrower distribution of RMSE. It can be observed that the model trained with 100 data of frequency samples achieves superior performance with the lowest median value (0.0125) of RMSE and the highest median value (28.68 dB) of PSNR, while the model trained with only one frequency sample has poor prediction as the highest median RMSE value of 0.0547 (increased by 337.6%) and the lowest median PSNR value of 16.3656dB (decreased by 12.3144dB) can be identified. The similar conclusion can be drawn from Figs. 15c and d that the manifold structure by 40 frequency samples appears highly separable as compared with the manifold by 5 frequency samples, and therefore the reconstruction using 40 frequency samples has more powerful learning ability to discriminate one type of defect from others.

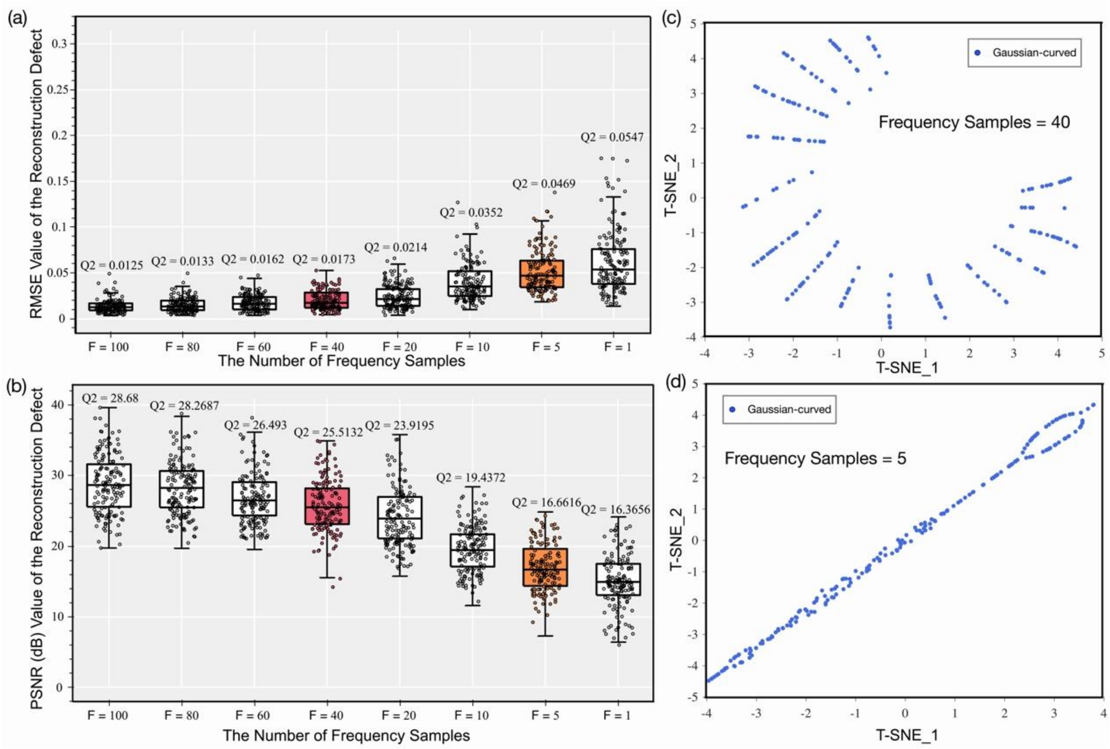

Fig. 15. Analysis of defect reconstruction for specific defects (Gaussian-curved defects) with different number of frequency samples. Boxplots of (a) RMSE and (b) PSNR values for each test set by models trained with different number of frequency samples; (c) Manifold structure of the input data set with (c) 40 and (d) 5 frequency samples.

Furthermore, it can be observed from the manifold structures in the aforementioned two cases that the manifold in the specific case has simpler and highly separable structure, thus it is simpler to empower the learning to realize higher reconstruction precision. A more direct quantitative comparison of the reconstruction performance of the trained general and specific models has been shown in Fig. 16. It is worth noting that the Deep-guide model trained for reconstructing specific defects can realize high precision just using comparatively fewer frequency samples. For example, it can be observed from Fig. 16 that the general model needs 40 frequency samples to reach the RMSE value of 0.026 or PSNR value of 22.426 dB, while only about 15 frequency samples for specific model are required. Overall, the superior robustness of the proposed Deep-guide framework has been demonstrated throughout two case studies. Also, defect reconstruction in the general case has the quality evaluated by the average RMSE value of 0.0388 and PSNR value of 20.0082 dB, whilst the values of RMSE and PSNR are much improved to 0.0272 by 42.65% and 23.1672 dB by 3.159 dB in specific case, respectively.

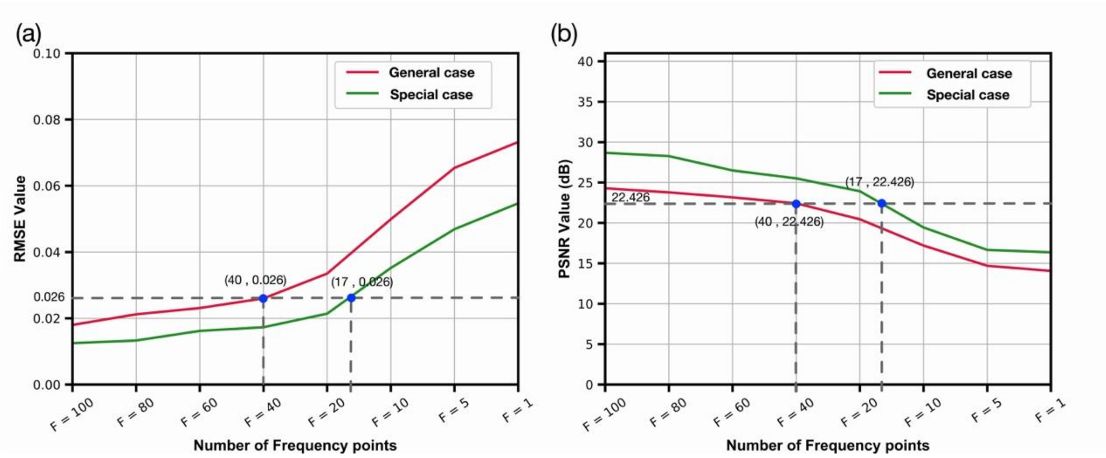

Fig. 16. (a) Comparison of the media RMSE on the entire test set from models trained with different number of frequency samples under two cases. (b) Comparison of the media PSNR on the entire test set from models trained with different number of frequency samples under two cases.

3.5 Effect of training data size on the accuracy of reconstruction

The major bottleneck for the application of deep learning to engineering is the limited size of available datasets. In non-destructive testing, the size of training data for data-driven model will directly affect the accuracy of defect detection and reconstruction. Taking into account this situation, it is necessary to investigate the impact of the size of the sample data on the reconstruction accuracy of the Deep-guide model, especially in the presence of small size samples.

First, the different size of sample data (data size $S = 600, 210, 30$) has been considered for constructing the Deep-guide models. To obtain the input data, 40 reflection coefficients in each defect reconstruction problem have been obtained by the wave analysis using $0th$ SH-waves mode. After the generation of the intelligent models, 450 unknown defects in test set have been examined using the trained models. Quantitative evaluations on test results in two case studies have been illustrated by boxplots shown in Fig. 17. As the size of training samples decreases, the reconstruction accuracy evaluated by RMSE or PSNR becomes poorer due to the limited learning information for training the Deep-guide network. For example, for defect reconstruction in general case, the model trained with 600 sampling data has the best performance with the lowest median value (0.0294) of RMSE, as compared with 0.0442 by the model trained with 210 sampling data (50.94% higher) or 0.0548 by the model 30 sampling data (86.39% higher). The similar conclusion can be drawn on the quality of the Deep-guide model assessed by the median value of

PSNR shown in Fig. 17b – the best result is $24.3416\ \mathrm{dB}$ by the model trained with 600 sample data, whilst $20.4234\ \mathrm{dB}$ with the net value of $3.9182\ \mathrm{dB}$ and $17.7327\ \mathrm{dB}$ with the net value of $6.6089\ \mathrm{dB}$ by the trained models using 210 and 30 sampling data, respectively. Moreover, it is evident that the Deep-guide model for reconstructing the specific defects shows better reconstruction performance, which is evaluated by a relatively lower and narrower distribution of RMSR or a relatively higher and narrower range of PSNR over the test dataset in Fig. 17. In summary, to reconstruct specific defects, a comparatively high-accuracy reconstruction can be achieved by the model with even few training data, which provide a useful insight into the development of data-driven techniques for engineering applications with small size of the training samples.

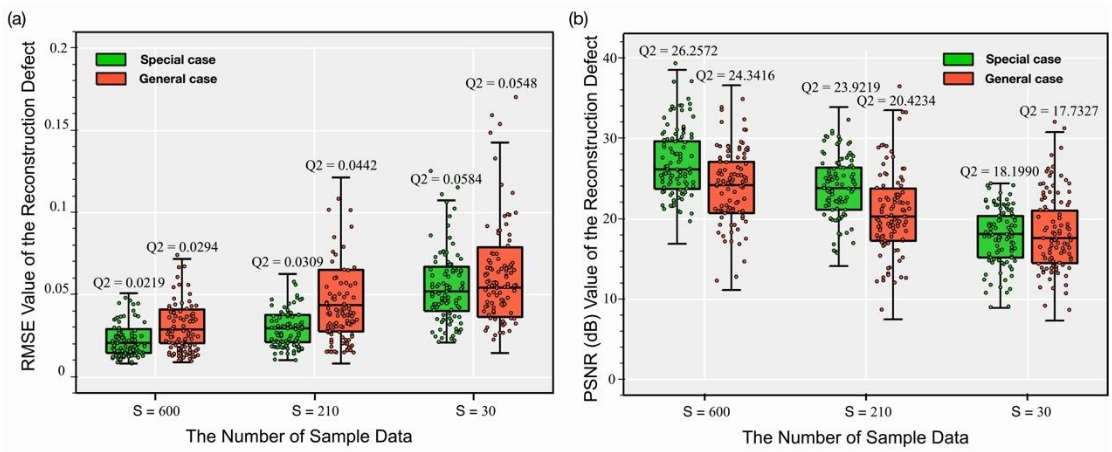

Fig. 17. Analysis the influence of the training data size on reconstruction performance in two cases. Boxplots of (a) RMSE values and (b) PSNR values for models trained by the different size of sampling data.

Furthermore, the correlation between the number of frequency samples and the size of sampling data has been investigated through the matrix view shown in Fig. 18. Influences of the number of frequency samples and the size of sampling data on the reconstruction accuracy of the Deep-guide framework has been indicated by the heatmap, which represents the RMSE or PSNR value of the item in the matrix. Deep-guide models have been trained by the different size of reflection coefficients, which have been obtained by the wave analysis using $0th$ SH-waves mode. Also, the number of circular frequency samples affecting the quality of defect reconstructs in general and specific cases has been studied. It has been noted that the larger the size of sampling data is used, the more the frequency samples are selected, the better the reconstruction quality is achieved. In practice, the amount of the available training data is usually small, and the defect reconstruction by fewer frequency samples takes benefits from less computational and experimental costs. Therefore, it is necessary to use as few training data and frequency samples as possible while meeting the reconstruction accuracy requirements. To better demonstrate the superiority of the proposed Deep-guide framework with an example, suppose that the defect reconstruction in Fig. 8 with the RMSE value less than 0.037 or the PSNR greater than $20\ \mathrm{dB}$ are deemed as the trustworthy quality within the acceptable tolerance. It can be observed in Fig. 18 that to reconstruct a defect in the specific case, at least 150 training defects and 20 frequency samples are required for the network training to meet the accuracy requirement, while to reconstruct a defect in the general case, at least 300 training defects and 40 frequency samples need to be satisfied for the qualified model construction. Thus, the Deep-guide model has the ability to solve the specific defect reconstruction problem with a high level of accuracy using small training samples and a small amount of frequency samples. Moreover, to achieve a certain level of reconstruction accuracy, either the increase of the number of training samples or more frequency samples can be adopted as a solution to the problem, and the decision-making depends on the types of resources available.

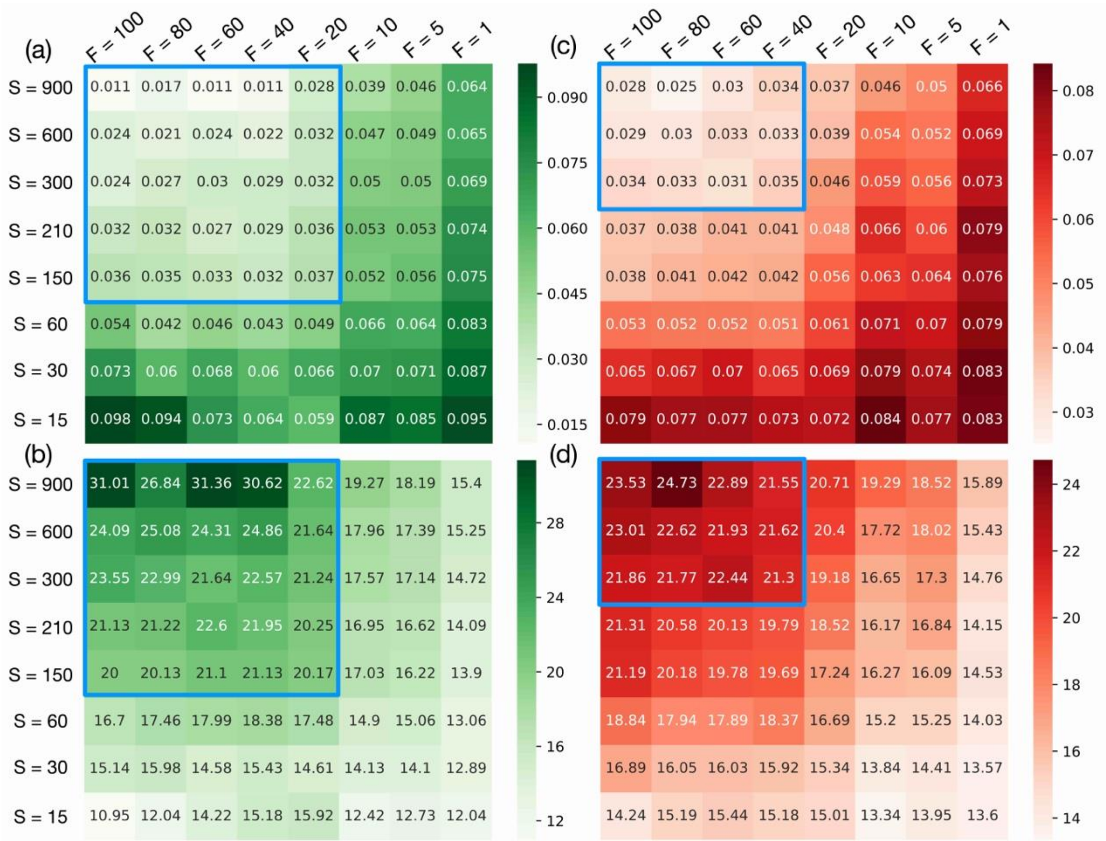

Fig. 18. A matrix view of the defect reconstruction accuracy against the different number of frequency samples and the different size of training data. Heatmap shows the distribution of reconstruction performance under different conditions. The blue box is the reconstruction accuracy that meets the accuracy criterion defined (RMSE $\leq$ 0.037 or PSNR $\geq$ 20dB). (a) Average RMSE and (b) PSNR of the entire test set (N=350) by models trained under different conditions in the specific case. (c) Average RMSE and (d) PSNR of the entire general test set (N=450) by models trained under different conditions in the general case.

4. Experimental Validation

4.1 Experimental setup for ultrasonic measurements

To validate the feasibility of the proposed reconstruction method, a circular array consisting of 32 Electromagnetic Acoustic Transducers (EMATs) has been designed in this research to perform experimental tests for defect reconstruction. Two aluminum plates with the dimension of $1200\ \mathrm{mm} \times 1200\ \mathrm{mm} \times 3\ \mathrm{mm}$ have been manufactured and an artificial circular defect has been intentionally created on the surface of each plate. The diameter and depth of the defect are set to 50 mm and 1 mm, respectively. One defect is located at the center of the plate $with\ the\ coordinate$ $(0, 0)$ mm, while the other is eccentrically placed with the coordinate $(100, 0)$ mm. The transducer parameters, including coil numbers and distances, have been carefully pre-adjusted to ensure the excitation creation of a relatively pure Lamb A0 mode with a central frequency of 250 kHz. Both the receiving and emitting probes have been manufactured using the advanced system, which comprises a signal generator (DG4062), power amplifier (RPR-4000), and oscilloscope (MS2024B) shown in Fig. 19a. A radial distance of 200 mm for the circular array has been deliberately used. During the process of experimental tests, the signal excitation has been generated at eight positions (Labels 1-5 and 29-32), as highlighted by the red dots in Fig. 19b. The signals have been then received by 32 probes (Labels 6-28). It should be noted that the data obtained from the receiving transducers in close proximity to the emitting points have been noticeably affected by unavoidable electromagnetic interference, leading to some inconsistent experimental data. Therefore, only data from the receiving transducers with Labels 6-28 have been deemed reliable. Overall, the final dataset has comprised 8 (emission signals) × 23 (receiving signals) matrix data.

In this study, the processing of the received signals has consisted of the following steps: First, the arrival time of the wave packet has been determined by the point with the highest energy flux density in the wavelet transform spectrum. Then, a three-period window centered around the arrival time has been selected to preserve the signal, while noise and unwanted reflected signals from other regions have been eliminated by setting to zeros. Following that, the truncated signal has been performed by fast Fourier transformation (FFT) to extract the signal value at 250 kHz in the frequency domain. This value has corresponded with the reflection coefficient mentioned in Eq. 12 and served as an input for subsequent reconstruction of defects using the proposed in the Deep-guide framework.

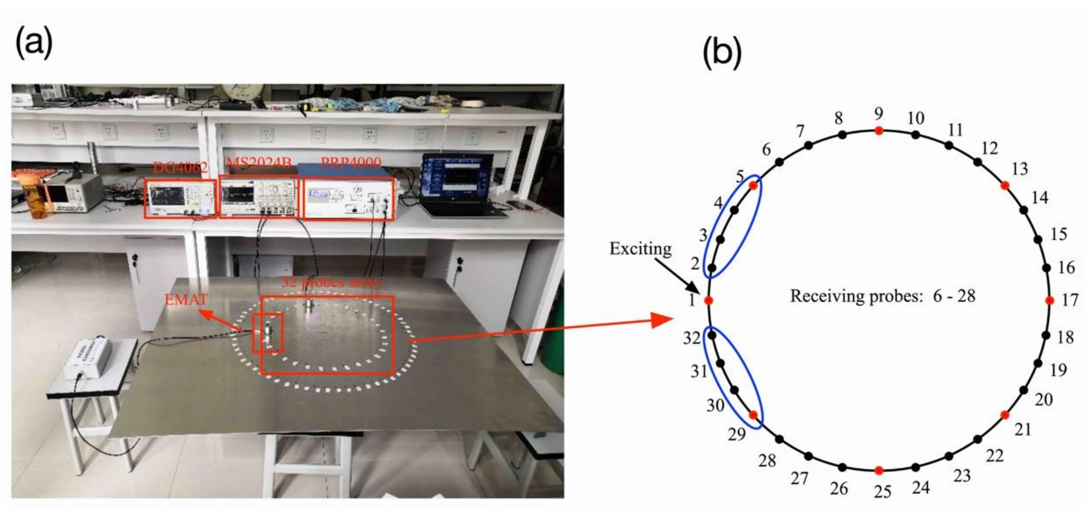

Fig. 19. (a) Experimental platform for electromagnetic ultrasonic non-destructive testing system. (b) Schematic diagram of EMATs array.

4.2 Experimental results

In this section, the neural network model has been trained using the simulation data from Section 3.3, which consists of 49 instances of circular defects with various sizes and positions. As a demonstration of, the experimental data obtained in Section 4.1 as the input to the network for reconstruction of circular defects has been used to verify the proposed Deep-guide. The output of the neural network has been formatted in a form of a matrix with the dimension of 400×400, containing a total number of 160,000 pixel values. Fig. 20 has illustrated the reconstructed results using the experimental data by the Deep-guide framework. It has been noted that Deep-guide has the ability to accurately predict the location of defects and the circular shape of the defects. In Fig.20 (c and d), the reconstruction by Deep-guide using the experimental data has not the same quality as that by the simulated data in Fig.8, for example, the RMSE of the experimental results (0.049) has increased by 87.02% and the PSNR (21.62dB) has been reduced to 3.25dB as compared to the results of A0 mode (RMSE=0.0262, PSNR=25.07dB) shown in Table 3. The main reasons can be explained as follows: 1) The experimental data contains environmental noise and human errors, which can affect the accuracy of the model trained by the simulation data; 2) Due to the electromagnetic interference, signals near the excitation probes cannot be reliably utilized, leading to a reduction in defect information provided to Deep-guide for reconstruction and thereby, decreasing the reconstruction accuracy; 3) In the experimental tests, only single-frequency scattered wave signals (250 KHz) have been used to improve the practicality of the experimental detection. However, as observed from the analysis results in Section 3.4, such signals have inevitably reduced the accuracy of the reconstruction. Overall, the experimental results have demonstrated that Deep-guide has the capability of extracting the accurate mapping relationship between defects and guided wave scattering signals through the training process on simulation data and its correctness has been also validated by the aforementioned experimental tests. The gained knowledge throughout this study has provided the opportunities to efficiently analyze and predict real-world measurements, enabling accurate reconstruction of defect positions and profiles.

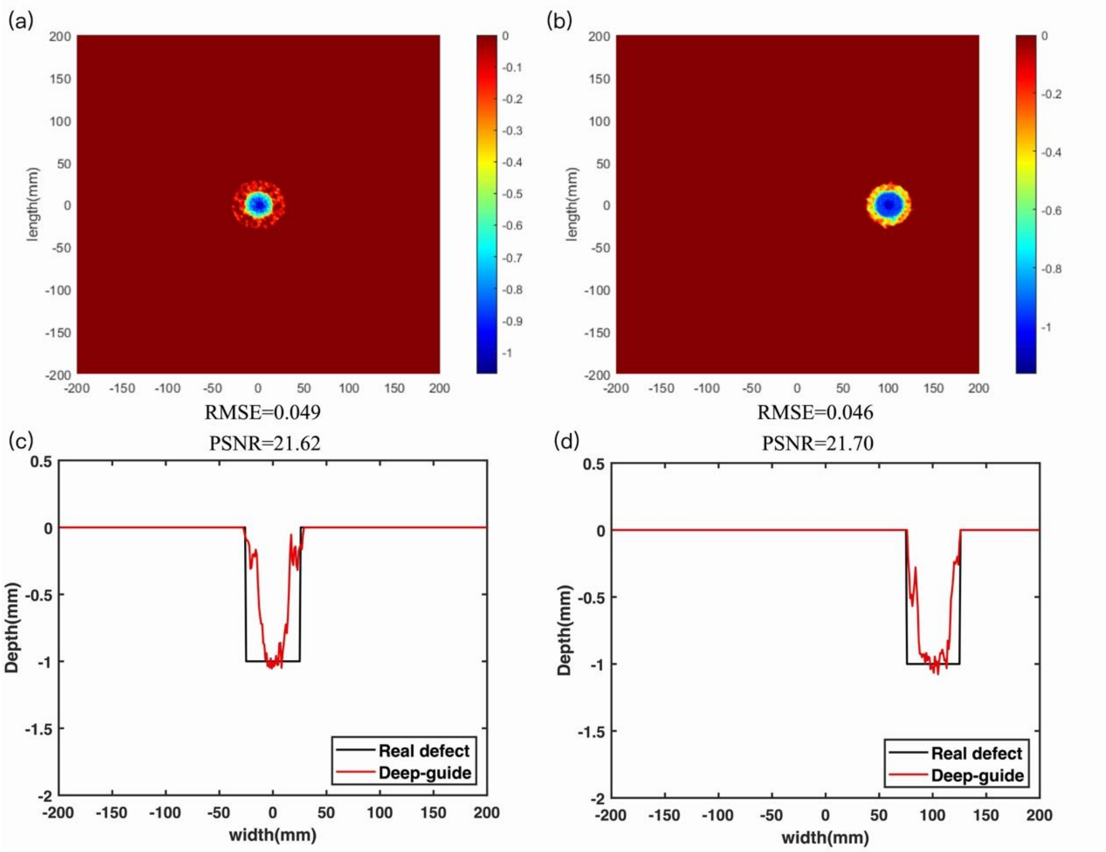

Fig. 20. Experimental results of defect reconstruction. Top view (a and b) and cross-sectional view (c and d) of the reconstructed results for central and eccentric defects, respectively.

5. Conclusions

Deep-guide, a novel data-driven structural defect reconstruction framework, has been proposed in this paper to automatically realize the end-end mapping between the transformed features of acoustic scattering signals and defect profiles with high levels of accuracy and efficiency. Based on the manifold distribution principle, the architecture of Deep-guide comprising the encoder-projection-decoder blocks has been designed and trained with the data generated by the developed modified boundary element method. To demonstrate the correctness, generality and efficiency of Deep-guide, numerical and experimental validations have been performed with the main conclusions as follows:

(1) Defect reconstructions using acoustic data generated by different modes of SH-waves and Lamb waves have demonstrated that Deep-guide has high levels of the accuracy, efficiency and generality.

(2) The manifold structure of the scattering data affects the reconstruction performance, that is to say, Deep-guide has the more powerful learning ability for data manifold being a simpler, highly separable structure, leading to the higher reconstruction accuracy.

(3) Through data training, a stochastic mapping that has the capability of adaptively denoising the scattering signals has been successfully learned, which indicates that Deep-guide has remarkable robustness and is able to effectively regularize the ill-posedness of the inverse guided wave scattering problem.

(4) As compared with traditional knowledge-driven reconstruction approaches, Deep-guide can effectively reconstruct the defects with fewer frequency samples, especially for the specific defect type in engineering. Deep-guide model enables the problem solving with a high level of accuracy under the presence of small-size training samples and provides a useful insight into the development of effective data-driven techniques for structural health monitoring and complex defect reconstructions.

Declaration of Competing Interest

None.

Acknowledgements

This work is supported by the National Natural Science Foundation of China (12061131013, 12211530064 and 12172171), the State Key Laboratory of Mechanics and Control of Mechanical Structures at NUAA (No. MCMS-E-0520K02), the Fundamental Research Funds for the Central Universities (Nos. NE2020002 and NS2019007), the National Natural Science Foundation of China for Creative Research Groups (No. 51921003), Postgraduate Research & Practice Innovation Program of Jiangsu Province (No. KYCX21_0184), the National Natural Science Foundation of Jiangsu Province (No. BK20211176), the Interdisciplinary Innovation Fund for Doctoral Students of Nanjing University of Aeronautics and Astronautics [No. KXKCXJJ202208] and a project funded by the Priority Academic Program Development of Jiangsu Higher Education Institutions (PAPD).

Corresponding authors

Correspondence to qianzh@nuaa.edu.cn and dianzi.liu@uea.ac.uk.

Availability of data and materials

The data that support the findings of this study are available on request from the corresponding author.

References

[1] Rose JL (2002) A baseline and vision of ultrasonic guided wave inspection potential. Journal of Pressure Vessel Technology 124(3):273-282. https://doi.org/10.1115/1.1491272

[2] Qing-Tian D, Chun YZ (2011) Propagation of guided waves in bonded composite structures with tapered adhesive layer[J]. Applied Mathematical Modelling 35(11):5369-5381. https://doi.org/10.1016/j.apm.2011.04.042

[3] Broda D, Staszewski WJ, Martowicz A, Uhl T, Silberschmidt VV (2014) Modelling of nonlinear crack–wave interactions for damage detection based on ultrasound—A review. Journal of Sound and Vibration 333(4):1097-1118. https://doi.org/10.1016/j.jsv.2013.09.033

[4] Hai B, Bause M, Kuberry PA (2019) Modeling concept and numerical simulation of ultrasonic wave propagation in a moving fluid-structure domain based on a monolithic approach. Applied Mathematical Modelling 75: 916-939. https://doi.org/10.1016/j.apm.2019.07.007

[5] Rose J, Pelts S, Cho Y (2000) Modeling for flaw sizing potential with guided waves. Journal of Nondestructive Evaluation 19(2):55-66. https://doi.org/10.1023/A:1006621308307

[6] Rose LRF, Wang CH (2004) Mindlin plate theory for damage detection: Source solutions. The Journal of the Acoustical Society of America 116(1):154-171. https://doi.org/10.1121/1.1739482

[7] Rose LRF, Wang CH (2010) Mindlin plate theory for damage detection: Imaging of flexural inhomogeneities. The Journal of the Acoustical Society of America 127(2):754-763. https://doi.org/10.1121/1.3277217

[8] Wang B, Hirose S (2012) Inverse problem for shape reconstruction of plate-thinning by guided SH-waves. Materials Transactions 53(10):1782-1789. https://doi.org/10.2320/matertrans.I-M2012823

[9] Wang B, Hirose S (2012) Shape reconstruction of plate thinning using reflection coefficients of ultrasonic lamb waves: A numerical approach. ISIJ International 52(7):1320-1327. https://doi.org/10.2355/isijinternational.52.1320

[10] Singh D, Castaings M, Bacon C (2011) Sizing strip-like defects in plates using guided waves. NDT & E International : Independent Nondestructive Testing and Evaluation 44(5):394-404. https://doi.org/10.1016/j.ndteint.2011.03.005

[11] Castaings M, Singh D, Viot P (2012) Sizing of impact damages in composite materials using ultrasonic guided waves. NDT & E International : Independent Nondestructive Testing and Evaluation 46(1):22-31. https://doi.org/10.1016/j.ndteint.2011.10.002

[12] Da Y, Dong G, Wang B, Liu D, Qian Z (2018) A novel approach to surface defect detection. International Journal of Engineering Science 133:181-195. https://doi.org/10.1016/j.ijengsci.2018.09.005

[13] Zhu F, Pan E, Qian Z, Wang Y (2019) Dispersion curves, mode shapes, stresses and energies of SH and lamb waves in layered elastic nanoplates with surface/interface effect. International Journal of Engineering Science 142:170-184. https://doi.org/10.1016/j.ijengsci.2019.06.003

[14] Arridge S, Maass P, Öktem O, Schönlieb C (2019) Solving inverse problems using

data-driven models. Acta Numerica 28:1-174. https://doi.org/10.1017/S0962492919000059
[15] Reader AJ, Corda G, Mehranian A, Costa-Luis CD, Ellis S, Schnabel JA (2021) Deep learning for PET image reconstruction. IEEE Transactions on Radiation and Plasma Medical Sciences 5(1) :1-25. https://doi.org/10.1109/TRPMS.2020.3014786
[16] Lecun Y, Bengio Y, Hinton G (2015) Deep learning. Nature (London) 521(7553):436-444. https://doi.org/10.1038/nature14539
[17] Xu K, Darve E (2021) Solving inverse problems in stochastic models using deep neural networks and adversarial training. Computer Methods in Applied Mechanics and Engineering 384(C):113976. https://doi.org/10.1016/j.cma.2021.113976
[18] Feng J, Teng Q, Li B, He X, Chen H, Li Y (2020) An end-to-end three-dimensional reconstruction framework of porous media from a single two-dimensional image based on deep learning. Computer Methods in Applied Mechanics and Engineering 368:113043. https://doi.org/10.1016/j.cma.2020.113043
[19] Tamaddon-Jahromi HR, Chakshu NK, Sazonov I, Evans LM, Thomas H, Nithiarasu P (2020) Data-driven inverse modelling through neural network (deep learning) and computational heat transfer. Computer Methods in Applied Mechanics and Engineering 369:113217. https://doi.org/10.1016/j.cma.2020.113217
[20] Pled F, Desceliers C, Zhang T (2021) A robust solution of a statistical inverse problem in multiscale computational mechanics using an artificial neural network. Computer Methods in Applied Mechanics and Engineering 373:113540. https://doi.org/10.1016/j.cma.2020.113540
[21] Chen H, Zhang Y, Kalra MK, Lin F, Chen Y, Liao P, Zhou J, Wang G (2017) Low-dose CT with a residual encoder-decoder convolutional neural network. IEEE Transactions on Medical Imaging 36(12):2524-2535. https://doi.org/10.1109/TMI.2017.2715284
[22] Zhu B, Liu JZ, Cauley SF, Rosen BR, Rosen MS (2018) Image reconstruction by domain-transform manifold learning. Nature (London) 555(7697):487-492. https://doi.org/10.1038/nature25988
[23] Häggström I, Schmidtlein CR, Campanella G, Fuchs TJ (2019) DeepPET: A deep encoder–decoder network for directly solving the PET image reconstruction inverse problem. Medical Image Analysis 54:253-262. https://doi.org/10.1016/j.media.2019.03.013
[24] Gao Y, Gao L, Li X (2021) A generative adversarial network based deep learning method for low-quality defect image reconstruction and recognition. IEEE Transactions on Industrial Informatics 17(5):3231-3240. https://doi.org/10.1109/TII.2020.3008703
[25] Piao G, Guo J, Hu T, Leung H, Deng Y (2019) Fast reconstruction of 3-D defect profile from MFL signals using key physics-based parameters and SVM. NDT & E International : Independent Nondestructive Testing and Evaluation 103:26-38. https://doi.org/10.1016/j.ndteint.2019.01.004
[26] Zhang B, Yang D, Hong X, Jin G (2022) Deep emulational semi-supervised knowledge probability imaging method for plate structural health monitoring using guided waves. Engineering with Computers 38(5):4151-4166. https://doi.org/10.1007/s00366-022-01711-9
[27] Song H, Yusa N (2021) Inverse analysis of low frequency electromagnetic signals for sizing local wall thinning using a multivariate probabilistic model. NDT & E International : Independent Nondestructive Testing and Evaluation 119:102417. https://doi.org/10.1016/j.ndteint.2021.102417
[28] Tenenbaum JB, De Silva V, Langford JC (2000) A global geometric framework for nonlinear

dimensionality reduction. Science (American Association for the Advancement of Science) 290(5500):2319-2323. https://doi.org/10.1126/science.290.5500.2319

[29] Lei N, An D, Guo Y, Su K, Liu S, Luo Z, Yau S, Gu X (2020) A geometric understanding of deep learning. Engineering (Beijing, China) 6(3):361-374. https://doi.org/10.1016/j.eng.2019.09.010

[30] Vincent P, Larochelle H, Bengio Y, Manzagol P (2008) Extracting and composing robust features with denoising autoencoders. Machine Learning, Proceedings of the Twenty-Fifth International Conference (ICML 2008), Helsinki, Finland, June 5-9, 2008. https://doi.org/10.1145/1390156.1390294

[31] Van Der Maaten L, Hinton G (2008) Visualizing data using t-SNE. Journal of Machine Learning Research 9:2579-2625.

[32] Roweis S T, Saul L K (2000) Nonlinear dimensionality reduction by locally linear embedding. Science (American Association for the Advancement of Science) 290(5500): 2323-2326. https://doi.org/10.1126/science.290.5500.2323

[33] De Silva V, Tenenbaum JB (2002) Global Versus Local Methods in Nonlinear Dimensionality Reduction. NIPS 2002: Proceedings of the 15th International Conference on Neural Information Processing Systems 2002:705-712.

[34] Cai J, Shi L, Qing XP (2013) A time-distance domain transform method for lamb wave dispersion compensation considering signal waveform correction. Smart Materials and Structures 22(10):105024. https://doi.org/10.1088/0964-1726/22/10/105024

[35] Marin L (2005) Detection of cavities in helmholtz-type equations using the boundary element method. Computer Methods in Applied Mechanics and Engineering 194(36):4006-4023. https://doi.org/10.1016/j.cma.2004.10.005

[36] Yang C, Wang B, Qian Z (2021) Three dimensional modified BEM analysis of forward scattering problems in elastic solids. Engineering Analysis with Boundary Elements 122:145-154. https://doi.org/10.1016/j.enganabound.2020.10.012

[37] Achenbach JD (2004) Reciprocity in Elastodynamics. Cambridge University Press.

[38] Da Y, Li Q, Wang B, Liu D, & Qian Z (2021) A more accurate reconstruction method for detecting large-depth defects in plates using SH guided waves. Acta Mechanica Solida Sinica 34(2): 174-183. https://link.springer.com/article/10.1007/s10338-020-00197-6